

Supersonic and Hypersonic Flows on 2D Unstructured Context: Part IV Other Turbulence Models

EDISSON SÁVIO DE GÓES MACIEL

Aeronautical Engineering Division (IEA)

Aeronautical Technological Institute (ITA)

Pça. Mal. do Ar Edurado Gomes, 50 – Vila das Acácias, 50 – São José dos Campos – SP – 12228-900
BRAZIL

edisavio@edissonsavio.eng.br <http://www.edissonsavio.br>

Abstract: - In this work, the fourth of this study, numerical simulations involving supersonic and hypersonic flows on an unstructured context are analyzed. The Van Leer and the Radespiel and Kroll schemes are implemented on a finite volume formulation, using unstructured spatial discretization. The algorithms are implemented in their first and second order spatial accuracies. The second order spatial accuracy is obtained by a linear reconstruction procedure based on the work of Barth and Jespersen. Several non-linear limiters are studied using the linear interpolation based on the work of Jacon and Knight. To the turbulent simulations, the Wilcox, the Menter and Rumsey and the Yoder, Georgiadis and Orkwis models are employed. The compression corner problem to the supersonic inviscid simulations and the re-entry capsule problem to the hypersonic viscous simulations are studied. The results have demonstrated that the Van Leer algorithm yields the best results in terms of the prediction of the shock angle of the oblique shock wave in the compression corner problem and the best value of the stagnation pressure at the configuration nose in the re-entry capsule configuration. The spatially variable time step is the best choice to accelerate the convergence of the numerical schemes, as reported by Maciel. In terms of turbulent results, the Wilcox model yields the best results, proving the good capacity of this turbulence model in simulate high hypersonic flows. This paper is continuation of Maciel's works started in 2011 and treats mainly the influence of turbulence models on the solution quality.

Key-Words: - Unstructured spatial discretization; Euler and Navier-Stokes equations; Van Leer algorithm; Radespiel and Kroll algorithm; Wilcox turbulence model; Menter and Rumsey turbulence model; Yoder, Georgiadis and Orkwis turbulence model.

1 Introduction

Conventional non-upwind algorithms have been used extensively to solve a wide variety of problems ([1]). Conventional algorithms are somewhat unreliable in the sense that for every different problem (and sometimes, every different case in the same class of problems) artificial dissipation terms must be specially tuned and judiciously chosen for convergence. Also, complex problems with shocks and steep compression and expansion gradients may defy solution altogether.

Upwind schemes are in general more robust but are also more involved in their derivation and application. Some upwind schemes that have been applied to the Euler equations are, for example, [2-4]. Some comments about these methods are reported below:

[2] suggested an upwind scheme based on the flux vector splitting concept. This scheme considered the fact that the convective flux vector components could be written as flow Mach number polynomial functions, as main characteristic. Such polynomials presented the particularity of having

the minor possible degree and the scheme had to satisfy seven basic properties to form such polynomials. This scheme was presented to the Euler equations in Cartesian coordinates and three-dimensions.

[3] proposed a new flux vector splitting scheme. They declared that their scheme was simple and its accuracy was equivalent and, in some cases, better than the [5] scheme accuracy in the solutions of the Euler and the Navier-Stokes equations. The scheme was robust and converged solutions were obtained so fast as the [5] scheme. The authors proposed the approximated definition of an advection Mach number at the cell face, using its neighbor cell values via associated characteristic velocities. This interface Mach number was so used to determine the upwind extrapolation of the convective quantities.

[4] emphasized that the [3] scheme had its merits of low computational complexity and low numerical diffusion as compared to other methods. They also mentioned that the original method had several deficiencies. The method yielded local pressure oscillations in the shock wave proximities, adverse

mesh and flow alignment problems. In the [4] work, a hybrid flux vector splitting scheme, which alternated between the [3] scheme and the [2] scheme, in the shock wave regions, was proposed, assuring that resolution of strength shocks was clear and sharply defined.

In this work, the fourth of this study, numerical simulations involving supersonic and hypersonic flows on an unstructured context are analysed. The [2, 4] schemes are implemented on a finite volume formulation, using unstructured spatial discretization. The algorithms are implemented in their first and second order spatial accuracies. The second order spatial accuracy is obtained by a linear reconstruction procedure based on the work of [6]. Several non-linear limiters are studied using the linear interpolation based on the work of [7]. To the turbulent simulations, the [8-10] models are employed. The compression corner problem to the inviscid simulations and the re-entry capsule problem to the hypersonic viscous simulations are studied. The results have demonstrated that the [2] algorithm yields the best results in terms of the prediction of the shock angle of the oblique shock wave in the compression corner problem and the best value of the stagnation pressure at the configuration nose in the re-entry capsule configuration. The spatially variable time step is the best choice to accelerate the convergence of the numerical schemes, as reported by [11-12]. In terms of turbulent results, the [8] model yields the best results, proving the good capacity of this turbulence model in simulate high hypersonic flows. This paper is continuation of Maciel's works started in 2011 and treats mainly the influence of turbulence models on the solution quality.

For more details about the motivation of this study as also literature revision, the reader is encouraged to read [13], the third part of this study.

2 Results

Following the studies restarted in [13], this paper continues to analyze the turbulent flow around a reentry capsule. For details of the geometry, mesh and boundary conditions, the reader is encouraged to see [13-14].

2.1 Turbulent Solutions – Same Sense Mesh Generation

Case 1 – $M = 7.0$ (Low “cold gas” hypersonic flow). Figures 1 and 2 present the pressure field obtained by [2, 4] schemes as using the [9] model,

in its Wilcox version. No differences are perceptible in relation to the [8] turbulence model, as expected. This version of the [9] turbulence model should repeat the [8] solution and is it what happens.

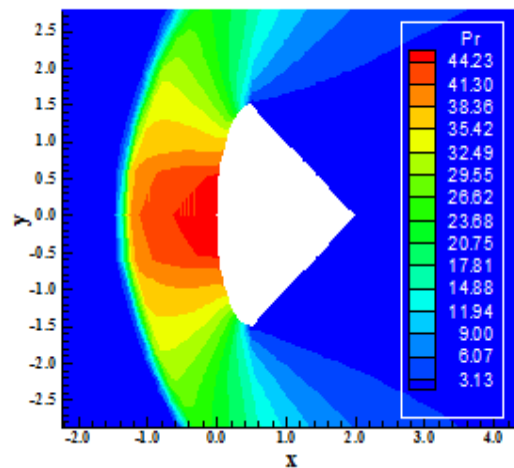


Figure 1. Pressure contours (VL-MR-W).

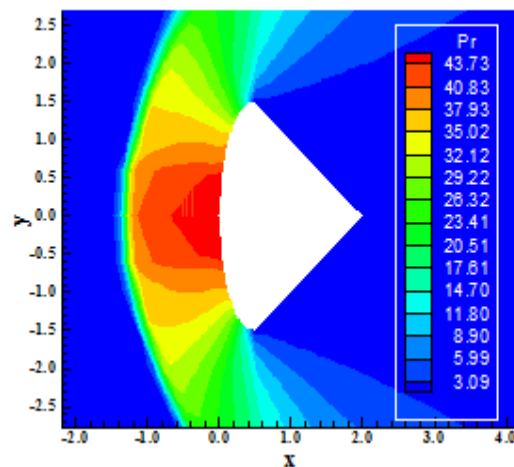


Figure 2. Pressure contours (RK-MR-W).

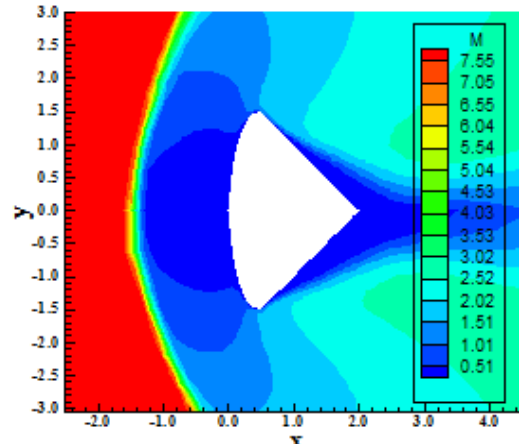


Figure 3. Mach number contours (VL-MR-W).

The pressure field generated by the [2] scheme is more strength than that generated by the [4] scheme. Good characteristics of symmetry are observed.

Figures 3 and 4 show the Mach number fields generated by [2, 4] schemes, respectively. Both solutions present the development of a wake at the trailing edge of the configuration. It indicates a great loss of energy due to boundary layer separation with the formation of a pair of circulation bubbles. The shock is well captured by the schemes.

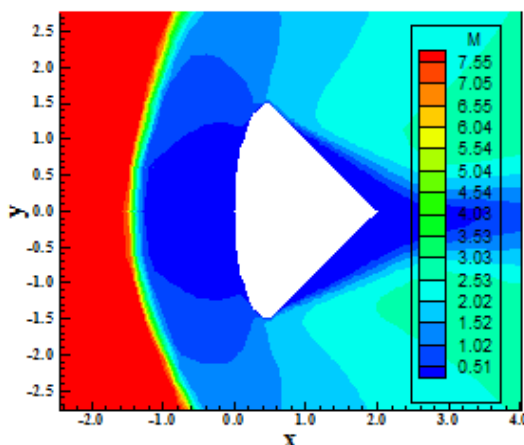


Figure 4. Mach number contours (RK-MR-W).

Figures 5 and 6 exhibit the velocity field and the streamlines at the trailing edge region of the re-entry body. As can be seen, the boundary layer separation is well captured by both schemes. The formation of a pair of circulation bubble is well captured by the algorithms. Good symmetry is observed, even in the SS case. The wake formation is not aligned with the body's symmetry axis, which indicates that this solution is not totally symmetrical.

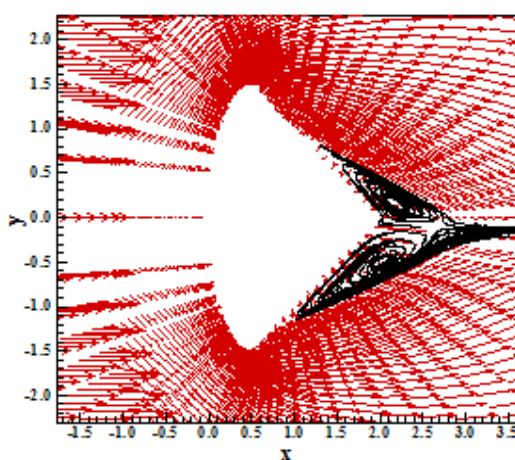


Figure 5. Velocity field and streamlines (VL-MR-W).

This aspect is expected because of the way that the mesh is generated, as aforementioned. For a zero attack angle, these streamlines should be aligned with the body's geometry axis. Qualitatively, there are some differences in this solution of [9] and in the solution of [8]. The wake captured by the former is minor than the wake captured by the latter, in both algorithms. It is an aspect of the turbulence models and not due to the algorithms. Apparently, the [39] turbulence model, in its Wilcox variant, does not yield any difference in relation to the [8] model. It is the expected comportment because this variant should reproduce the behavior of the original [8] model. It is expected that the other variants of the [9] turbulence model yields a different behavior.

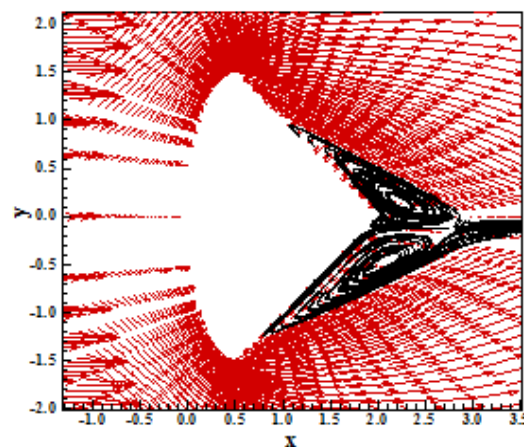


Figure 6. Velocity field and streamlines (RK-MR-W).

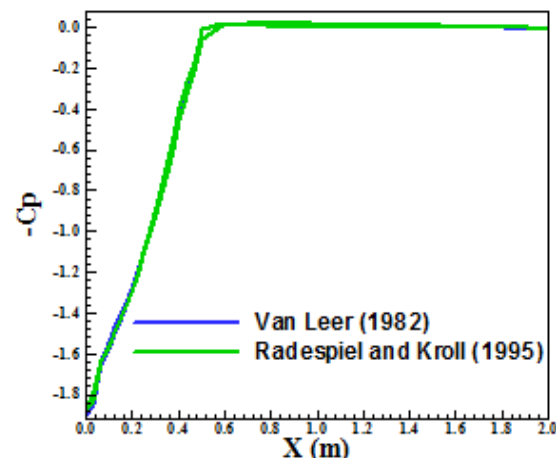


Figure 7. $-C_p$ distributions at wall.

Figure 7 presents the $-C_p$ distribution calculated around the re-entry capsule configuration. There are not meaningful differences between the two solutions: [2, 4] solutions. The $-C_p$ plateau indicates that approximately, after $x = 0.6\text{m}$, the pressure stay constant and equal to the freestream value. This is the region of boundary layer

separation and indicates that this region, of great energy exchange, is submitted at the environment pressure value out of the shock layer. It satisfies the boundary layer theory that presumes a pressure gradient close to zero at this region ($dp/dy = 0$). However, this is the expected behavior for an attached boundary layer. For a detached boundary layer, with the formation of circulation bubbles, it was expected not be more valid. The C_p peak at the re-entry capsule leading edge assumes the value of 1.92, as was the value obtained by the [8] model.

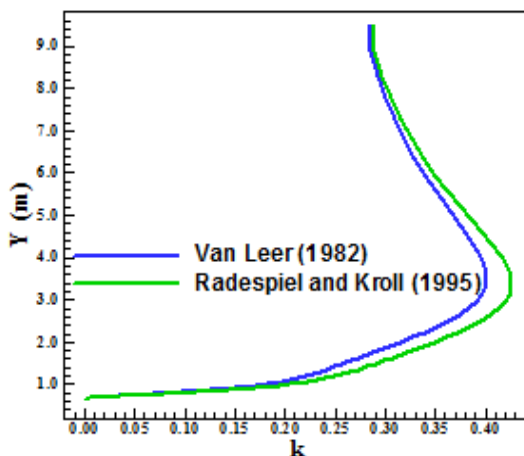


Figure 8. Turbulent kinetic energy.

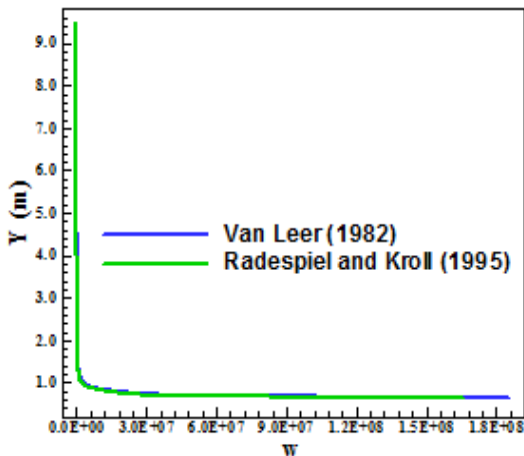


Figure 9. Turbulent vorticity.

Figure 8 and 9 show the turbulent kinetic energy and the turbulent vorticity profiles at node 58 (at the re-entry surface), respectively, generated by the [2, 4] algorithms. Again, the [4] algorithm captures more energy of the mean flow and increases the turbulent kinetic energy. The dissipation of the mean flow energy is also plotted to the two algorithms. The vorticity field is about 10 times greater than the respective field calculated with the [8] model.

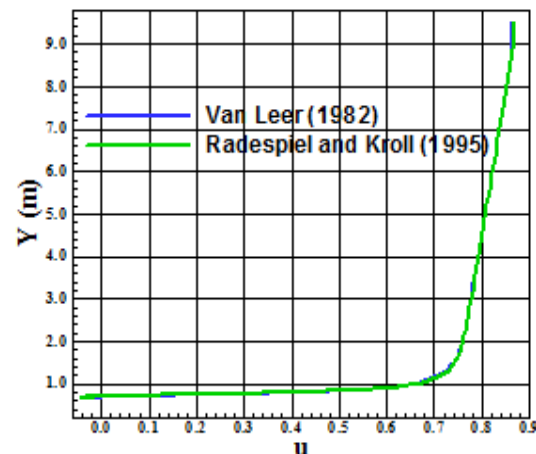


Figure 10. u profile.

Figure 10 shows the dimensionless u profile. It presents the characteristic behavior of a turbulent boundary layer. It presents a reverse flow close to the wall.

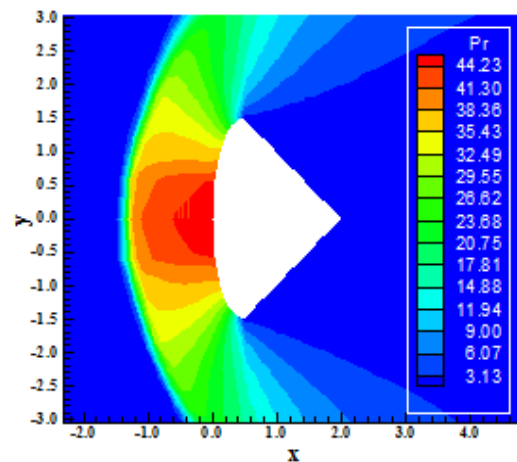


Figure 11. Pressure contours (VL-MR-TL).

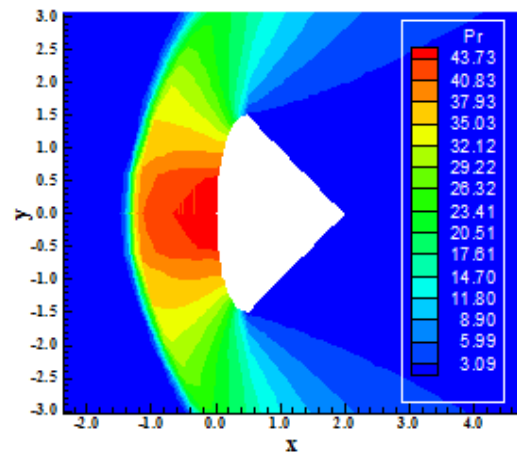


Figure 12. Pressure contours (RK-MR-TL).

Figure 11 and 12 exhibit the pressure contours generated by the [2, 4] schemes to the re-entry capsule problem. They apply the [9] turbulence model in its two-layers variant to simulate turbulent aspects of the flow. As can be noted, the pressure field generated by the [2] scheme is again more strength than the respective one generated by the [4] scheme. This behavior was observed in all solutions analyzed until now.

Figures 13 and 14 show the Mach number contours obtained by [2, 4] algorithms. Both solutions present a Mach number peak greater than that of the simulation in the freestream. Both solutions also capture the shock wave at the body leading edge and the wake at the body trailing edge. The Mach number field presents a good symmetry behavior at the leading edge region, but this field at the trailing edge is clearly non-symmetric.

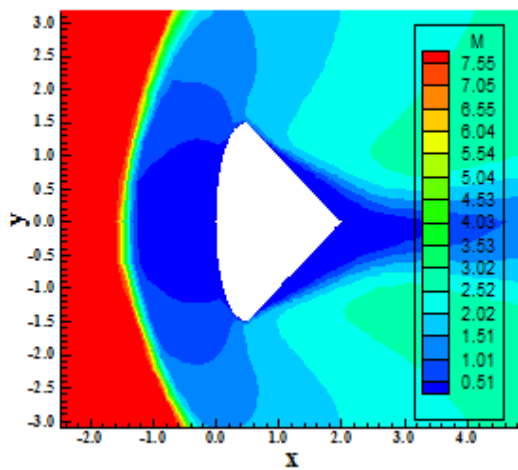


Figure 13. Mach number contours (VL-MR-TL).

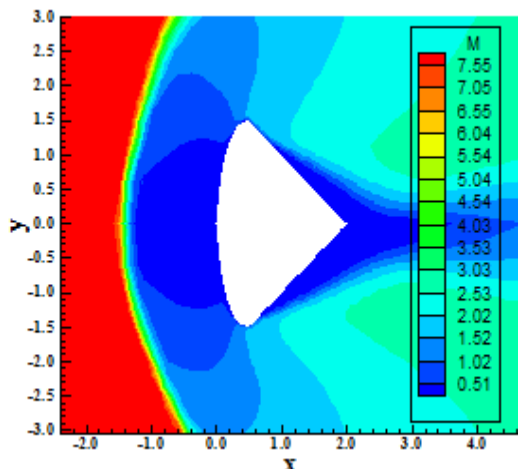


Figure 14. Mach number contours (RK_MR-TL).

As observed in the other turbulence models, this aspect can be due to the mesh generation process, as

seen in [14], or could be a problem of the choice turbulence model. Until now, it seems that the problem of the mesh generation process is the responsible by this non-symmetric behavior.

Figures 15 and 16 present the velocity field and the streamlines obtained by the [2, 4] schemes, respectively. As can be observed, the separation boundary layer and the formation of a pair of circulation bubbles are captured by both schemes. There is the formation of a wake at the body's trailing edge which is detected by the [2, 4] schemes. The adherence and impermeability conditions are well satisfied above of this separation region by both algorithms. The non-symmetry seems to be more critical in the [4] scheme.

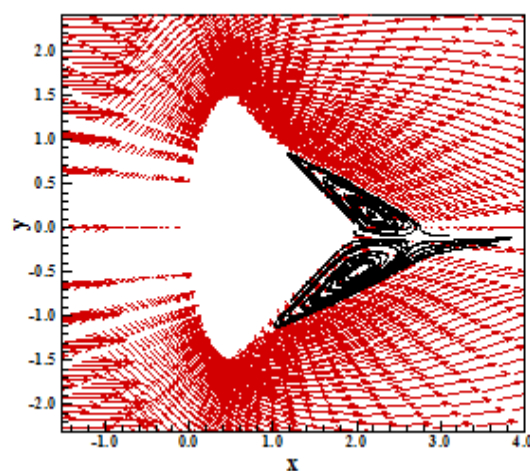


Figure 15. Velocity field and streamlines (VL-MR-TL).

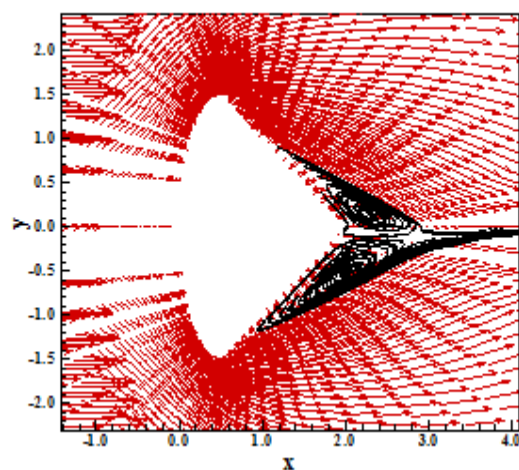


Figure 16. Velocity field and streamlines (RK-MR-TL).

Figure 17 exhibits the $-C_p$ distributions at wall generated by the [2, 4] schemes. As in the other cases, there are not meaningful discrepancies between the solutions. The C_p peak has a value of 1.92, equal to the other cases. Figures 18 and 19 present the turbulent kinetic energy and the

turbulent vorticity profiles at node 58. The turbulent kinetic energy profile shows the same of the cases aforementioned: the [4] scheme absorbs energy from the mean flow and transforms it in turbulent kinetic energy through the energy cascade. The dissipation rates are bigger than those obtained with the [8] model (more less 10 times). The great part of the dissipation of energy by the flow vortices occurs close to the wall, as expecting. Values of vorticity as high as 10^8 are obtained by the numerical algorithms using this two-layers version of the [9] turbulence model.

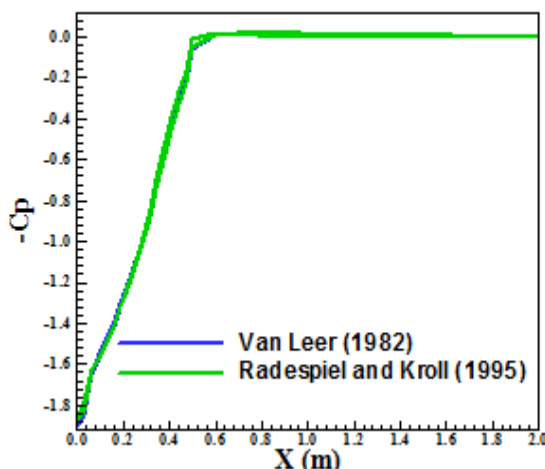


Figure 17. $-C_p$ distributions at wall.

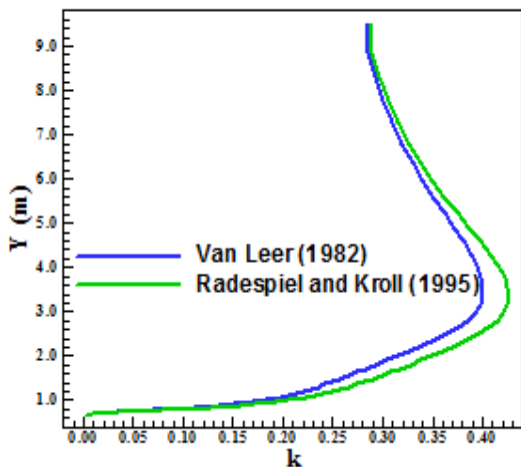


Figure 18. Turbulent kinetic energy.

Figure 20 shows the u profile at node 58. The boundary layer is fully turbulent because u presents a flat form close to the wall and a fast increase in direction to this frontier.

Figures 21 and 22 exhibit the pressure contours obtained by the [2, 4] schemes employing the [9] turbulence model in their BSL version. As can see, no significant differences exist in these solutions in

comparison with the others. The [2] pressure solution is again more severe than the [4] pressure solution, characterizing the former as more conservative.

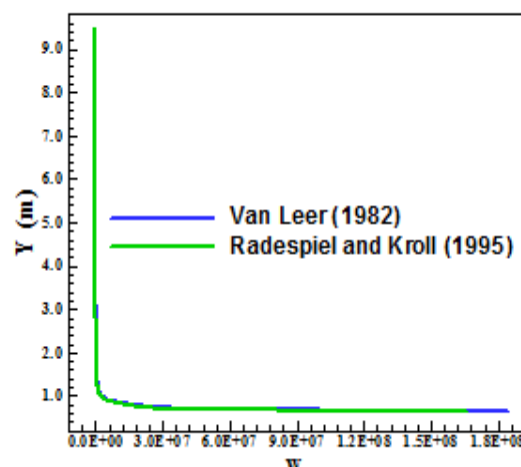


Figure 19. Turbulent vorticity.

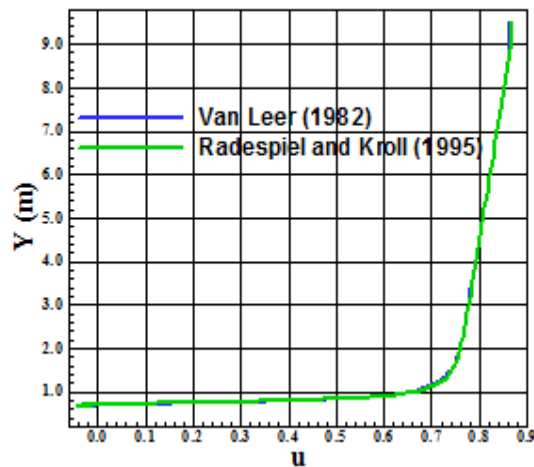


Figure 20. u profile.

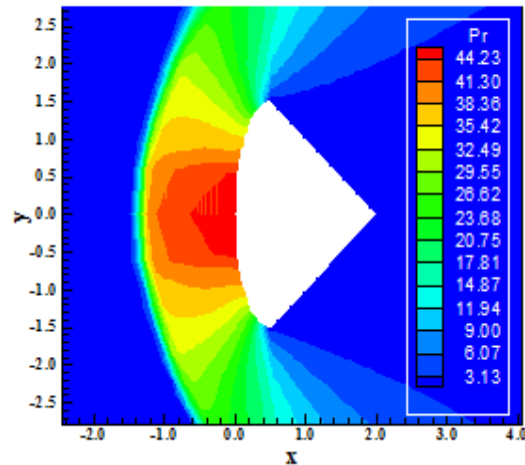


Figure 21. Pressure contours (VL-MR-BSL).

Figures 23 and 24 show the Mach number contours obtained by the [2, 4] schemes, respectively, when using the BSL version of the [9] turbulence model. As can be noted, the non-symmetry continues present in the Mach number contours, mainly at the trailing edge, where a wake is formed. As said before, this wake is caused by a detachment of the boundary layer and the formation of a pair of vortices. Figures 25 and 26 exhibit the velocity field and the streamlines at the trailing edge of the re-entry capsule generated by the [2, 4] schemes, respectively. Both solutions capture appropriately the boundary layer separation and the formation of a pair of circulation bubbles that is developed at the trailing edge. The non-symmetry in these figures is clear.

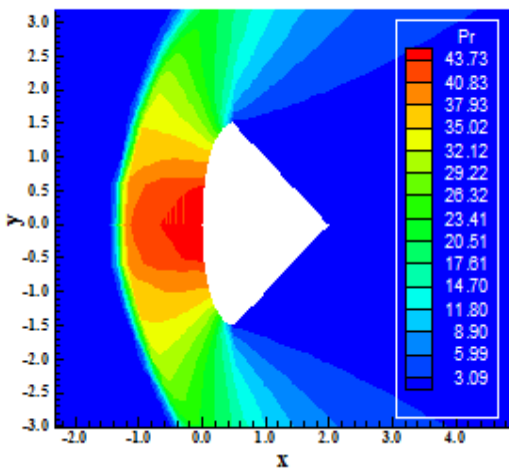


Figure 22. Pressure contours (RK-MR-BSL).

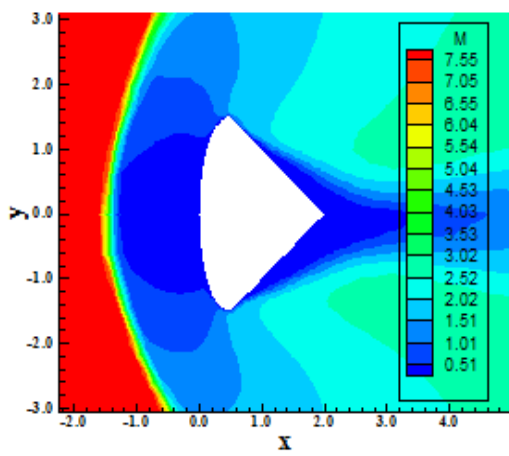


Figure 23. Mach number contours (VL-MR-BSL).

Figure 27 shows the $-C_p$ distribution at wall generated by each scheme. As can see, there are no meaningful differences between the curves. The plateau at the separation region is again obtained. The boundary layer condition of $dp/dy = 0$ is

assured. The C_p peak is again 1.92. Figure 28 exhibits the turbulent kinetic energy profile obtained from the [2, 4] algorithms. Some differences exist between the curves. The conversion of the mean flow kinetic energy into the turbulent kinetic energy has its biggest exchange in about 3.0m.

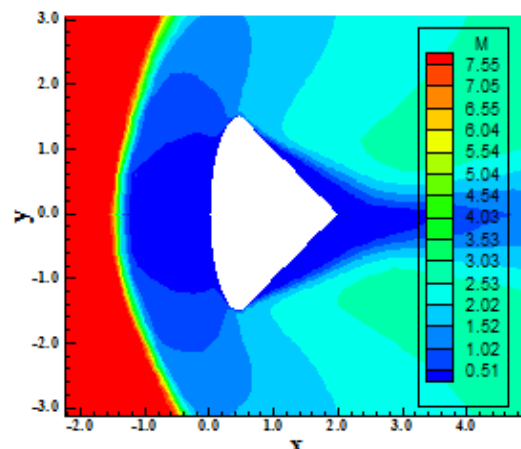


Figure 24. Mach number contours (RK-MR-BSL).

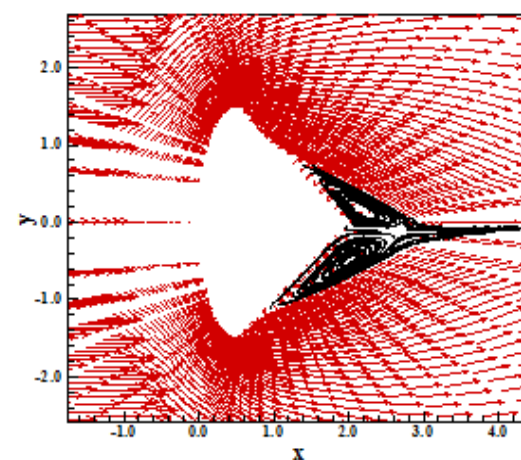


Figure 25. Velocity field and streamlines (VL-MR-BSL).

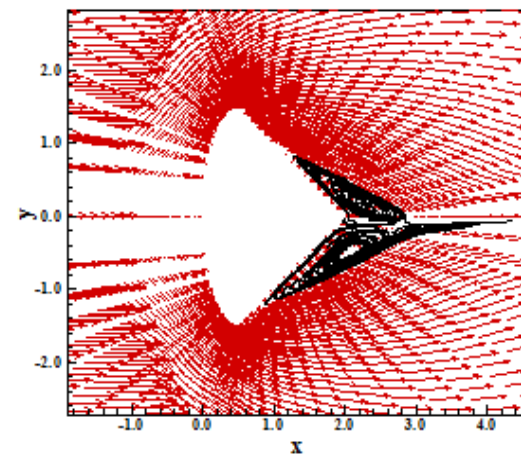


Figure 26. Velocity field and streamlines (RK-MR-BSL).

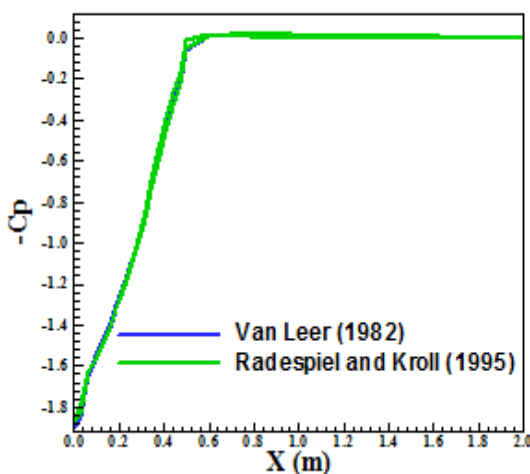
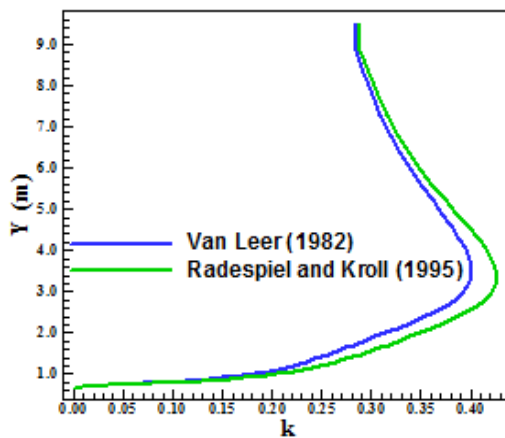
Figure 27. $-C_p$ distributions at wall.

Figure 28. Turbulent kinetic energy.

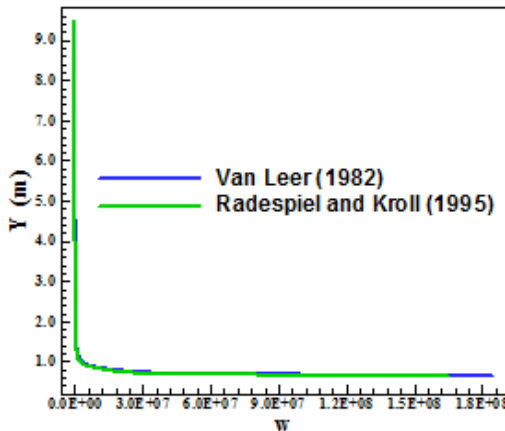


Figure 29. Turbulent vorticity.

Figure 29 presents the turbulent vorticity profile generated by [2, 4] schemes. As can be seen, the maximum dissipation rate reaches a dimensionless value of 2×10^8 . In all solutions presented herein, the vorticity reaches its maximum close to the wall, as expected. Out of the boundary layer, the vorticity is

zero, due to the location of the vortices is at wall.

Figure 30 shows the u profile at node 58. As seen, the u profile is typically of a turbulent boundary layer and is obtained by both algorithms.

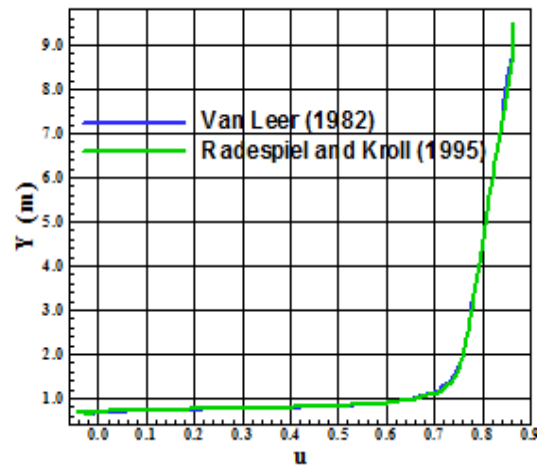


Figure 30. u profile.

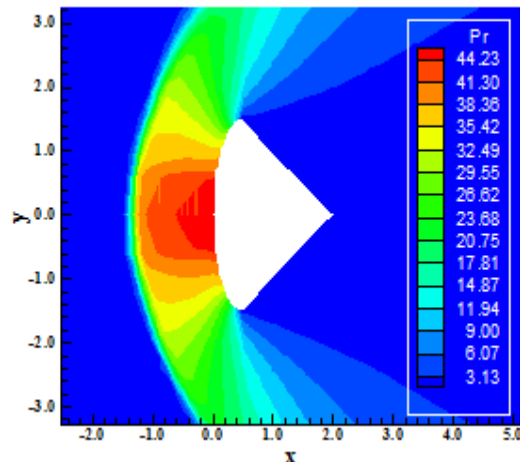


Figure 31. Pressure contours (VL-MR-SST).

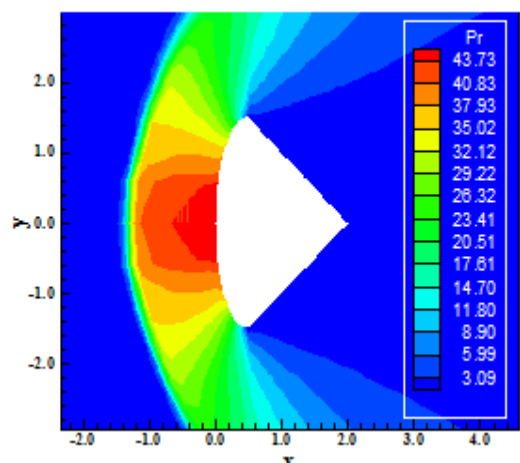


Figure 32. Pressure contours (RK-MR-SST).

Figures 31 and 32 show the pressure contours generated by the [2, 4] algorithms using the [9] turbulence model in their SST (“Shear Stress Transport”) version. The pressure distributions do not present any differences in relation to the other versions of the [9] model and in relation to the [8] model.

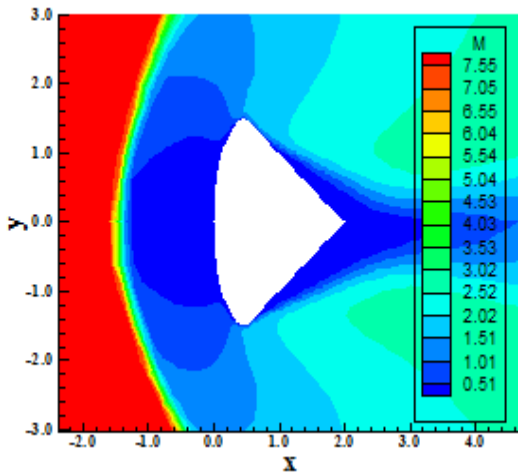


Figure 33. Mach number contours (VL-MR-SST).

Figures 33 and 34 present the Mach number contours generated by the [2, 4] schemes, respectively. Both solutions present the typical non-symmetry at the trailing edge, more specifically at the wake. Both algorithms capture accurately the shock wave.

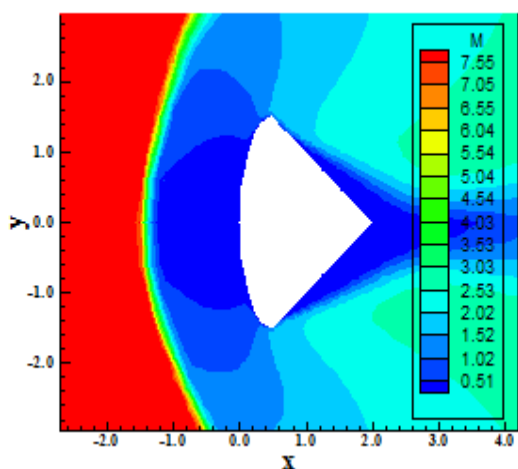


Figure 34. Mach number contours (RK-MR-SST).

Figures 35 and 36 show the velocity field and the streamlines at the trailing edge of the re-entry capsule generated by the [2, 4] schemes. Both solutions capture appropriately the boundary layer separation and the formation of a pair of circulation bubbles that is developed at the trailing edge. The

non-symmetry in these figures is clear. The wake is not aligned with the $y = 0.0$ axis. It is expected that with the alternated mesh generation process this non-symmetry be reduced or even disappear.

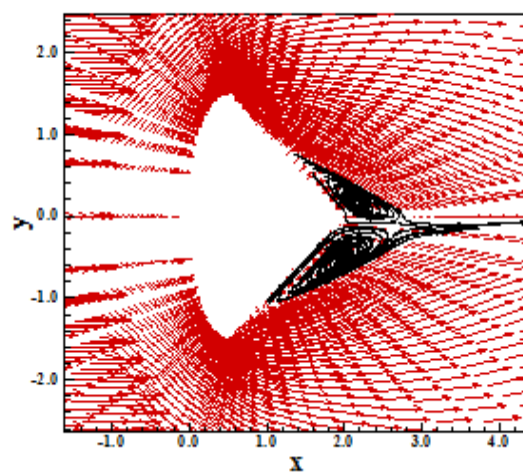


Figure 35. Velocity field and streamlines (VL-MR-SST).

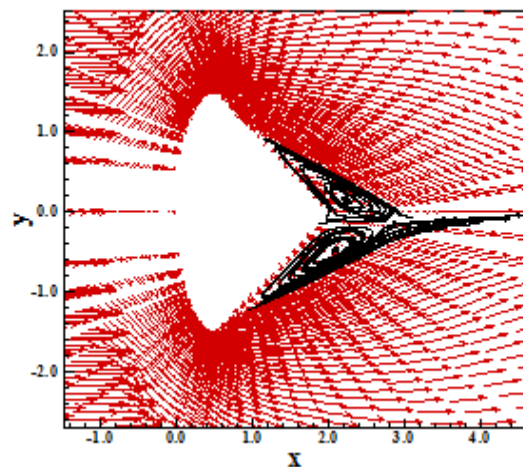


Figure 36. Velocity field and streamlines (RK-MR-SST).

Figure 37 presents the $-C_p$ distribution at wall generated by the [2, 4] schemes. Both solutions predict the same pressure or C_p plateau. No significant differences exist between the solutions.

Figures 38 and 39 exhibit the turbulent kinetic energy and the turbulent vorticity profiles, respectively, obtained by the numerical schemes. The turbulent kinetic energy profile at node 58 maintains the same characteristics of the other similar results. The turbulent vorticity presents a maximum peak close to 2×10^8 . The maximum values of the turbulent vorticity occur close to the wall due to the intense exchange of energy of the vortices in this location.

Figure 40 presents the u profile at node 58. The turbulent profile of velocity is characterized in this figure; in other words, the velocity profile of Fig. 40

is a typical one of the turbulent flow, being flat close to the wall and having a significant increase as the boundary edge is reached.

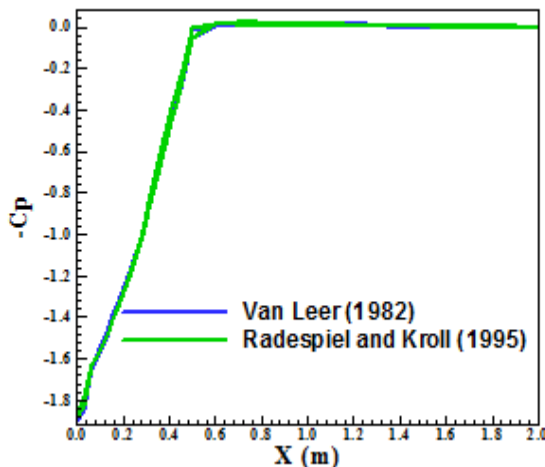


Figure 37. $-C_p$ distributions at wall.

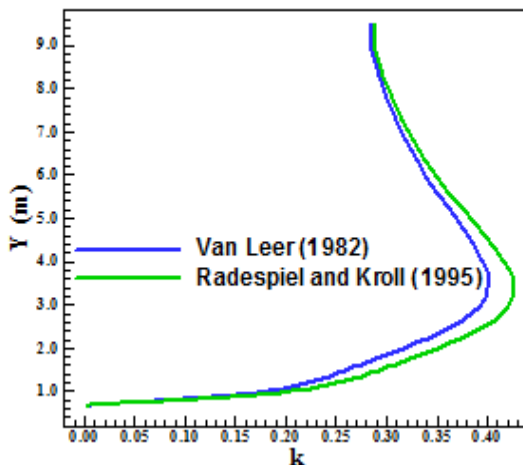


Figure 38. Turbulent kinetic energy.

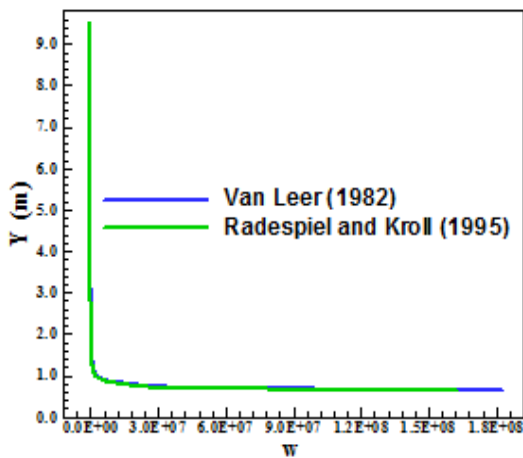


Figure 39. Turbulent vorticity.

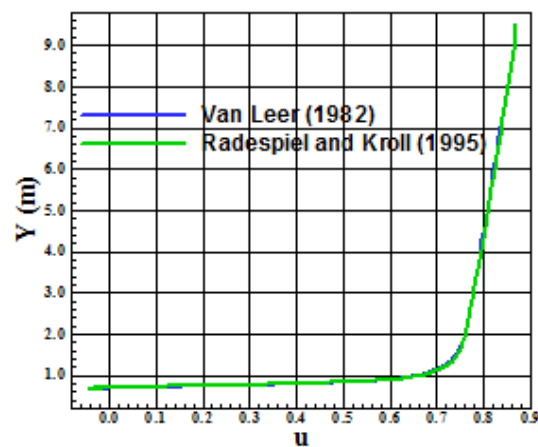


Figure 40. u profile.

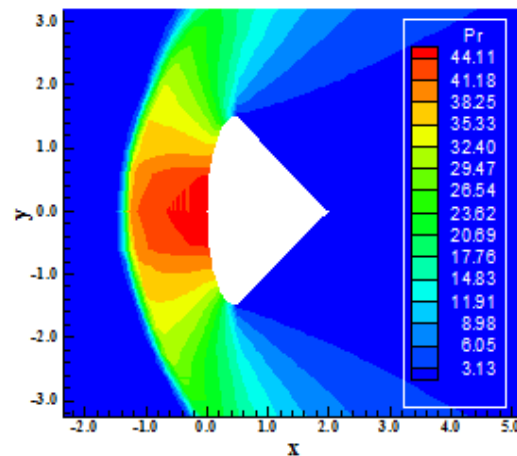


Figure 41. Pressure contours (VL-YGO).

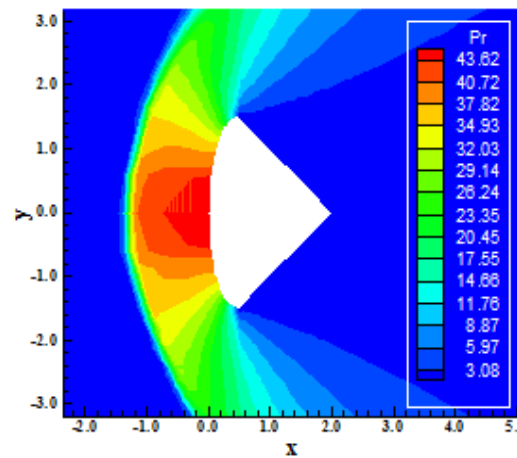


Figure 42. Pressure contours (RK-YGO).

Figures 41 and 42 exhibit the pressure contours obtained by [2, 4], respectively, employing the turbulence model of [10]. As can be seen, the pressure field generated by the [2] algorithm is more strength than the respective one generated by the [4]

algorithm. The results present good symmetry properties and free of oscillations. In relation to the respective solutions with the [8] and with [9], in all versions, there is no significant difference. Only the upper-levels of the legend suffered displacement.

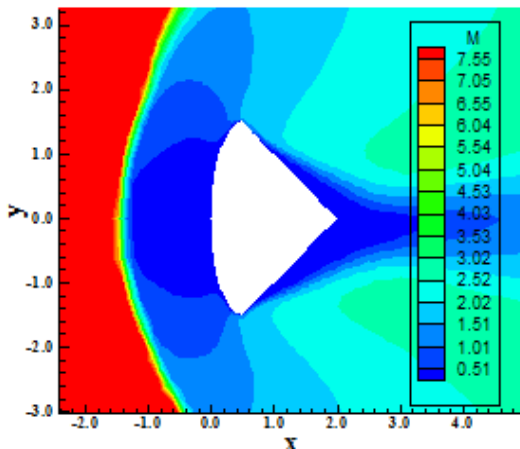


Figure 43. Mach number contours (VL-YGO).

Figures 43 and 44 show the Mach number contours obtained by the [2, 4] schemes, respectively, as using the turbulence model of [10]. The non-symmetry region at the wake is again observed as using this turbulence model. The [2] solution seems to be more asymmetric.

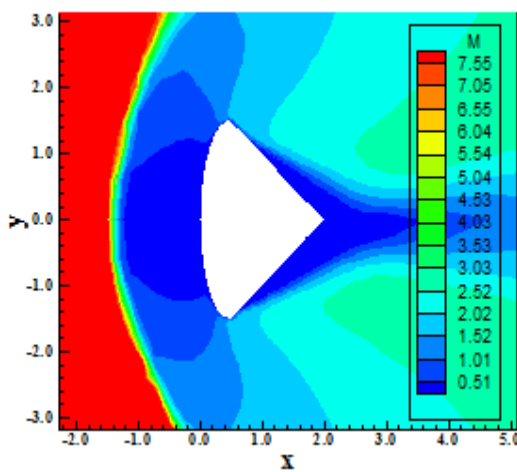


Figure 44. Mach number contours (RK-YGO).

Figures 45 and 46 present the velocity field and the streamlines around the re-entry capsule obtained by [2, 4] algorithms. As can see, the solutions indicate the formation of a pair of vortices. These vortices are distributed in space in an asymmetric disposition, typical of SS mesh generation process. This fact is the responsible to the non-symmetric distribution of the wake in space.

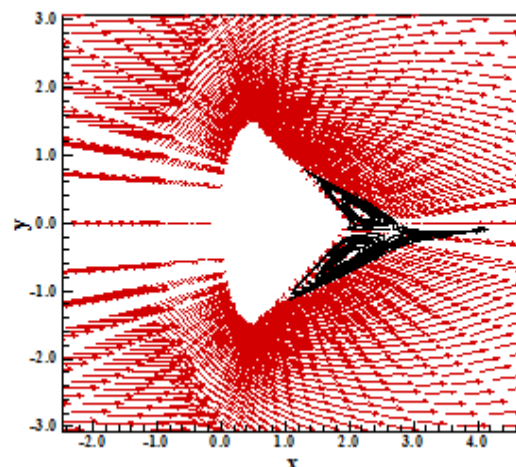


Figure 45. Velocity field and streamlines (VL-YGO).

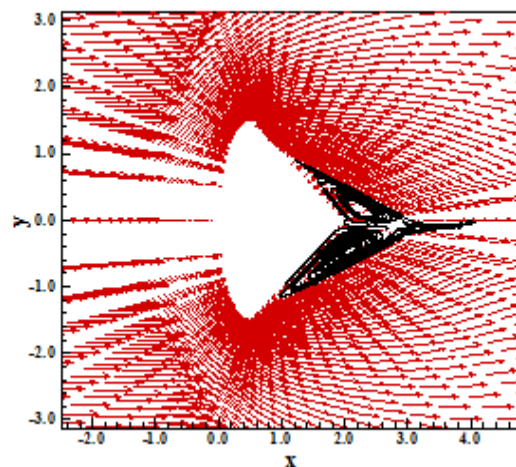


Figure 46. Velocity field and streamlines (RK-YGO).

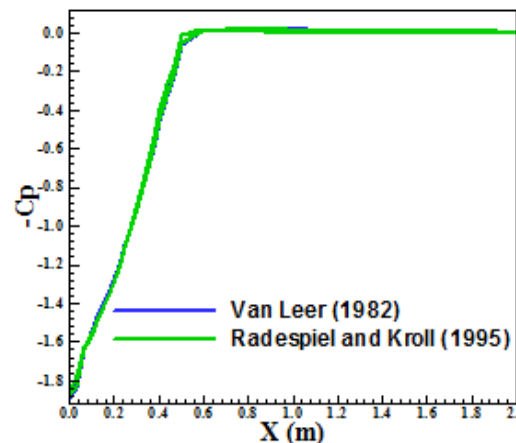


Figure 47. –Cp distributions at wall.

Figure 47 presents the wall pressure distribution generated by the [2, 4] algorithms. As can see, there are no meaningful differences. The pressure plateau was well captured and the peak of C_p has the value of 1.92. These solutions of the [10] turbulence

model agree practically totally with the others solutions presented at this work.

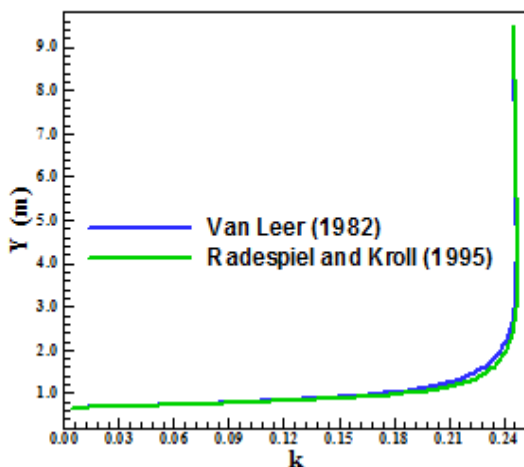


Figure 48. Turbulent kinetic energy.

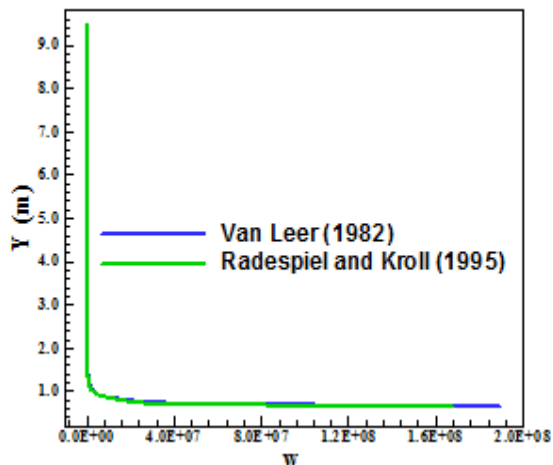


Figure 49. Turbulent vorticity.

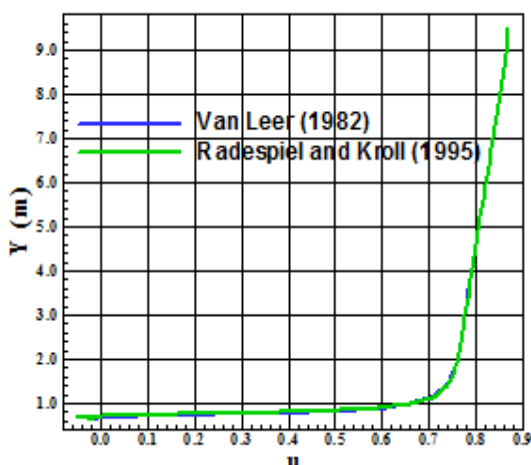


Figure 50. u profile.

Figures 48 and 49 show the turbulent kinetic energy and the turbulent vorticity profiles at node 58. A significant difference is observed in the kinetic energy profile. It presents a smooth behavior until $y = 3.0\text{m}$. After that, k assumes the constant value of 0.25 (dimensionless). Figure 116 exhibits the turbulent vorticity profile. It is possible to note that again the maximum occurs close to the wall. The peak of turbulent vorticity is about 2×10^8 .

Figure 50 shows the u profile. The behavior of the u profile is typical of turbulent boundary layers, even with separation.

Case 2 – $M = 9.0$ (Moderate “cold gas” hypersonic flow). Figures 51 and 52 show the pressure contours obtained by the [2, 4] schemes using the [8] turbulence model. The pressure field obtained by the [2] scheme is more severe than the respective of the [4] scheme, characterizing the former as more conservative. Good symmetry properties are observed.

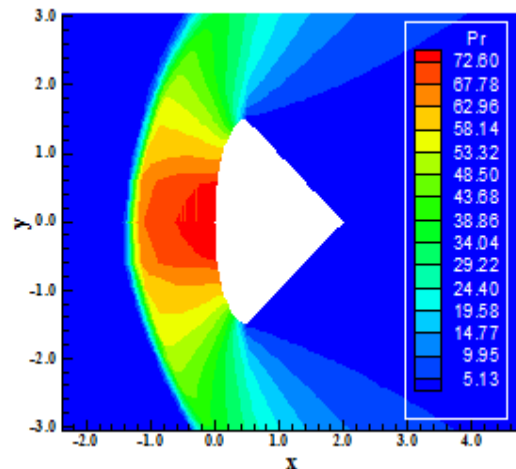


Figure 51. Pressure contours (VL-W).

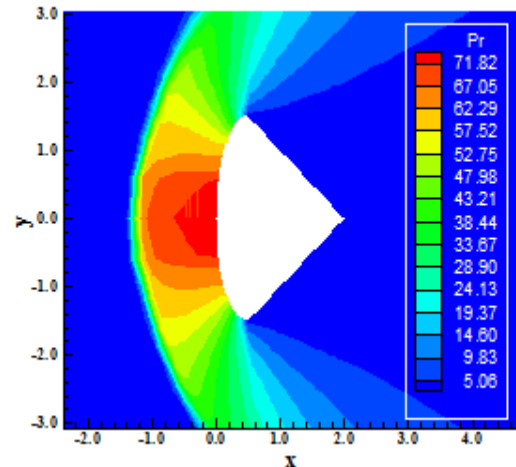


Figure 52. Pressure contours (RK-W).

Figures 53 and 54 present the Mach number contours generated by the [2, 4] schemes, respectively. Both algorithms over-predict the Mach number field. The peak of Mach number field should be 9.0 and not 10.94. The wake presents a non-symmetrical behavior yet. The shock wave is well captured by both methods.

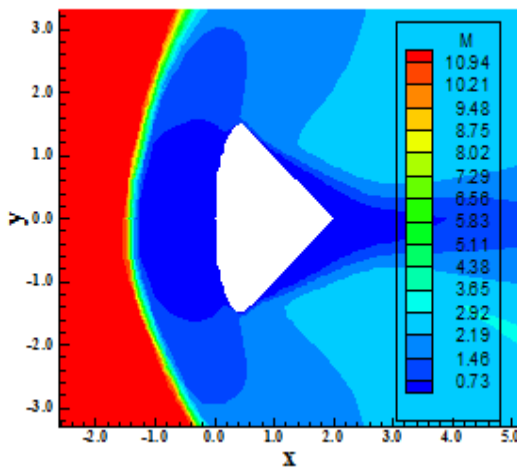


Figure 53. Mach number contours (VL-W).

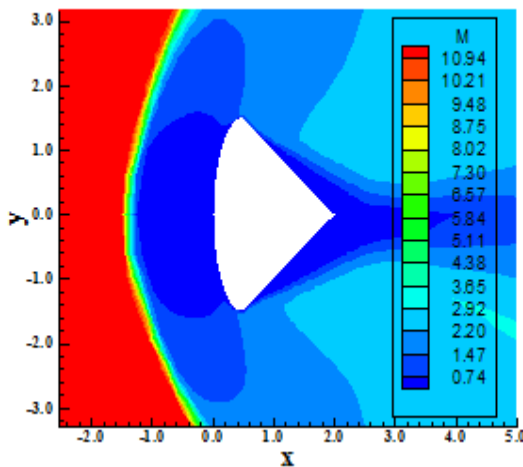


Figure 54. Mach number contours (RK-W).

Figures 55 and 56 presents the velocity field and the streamlines generated by the [2, 4] schemes, respectively, using the [8] turbulence model. A pair of vortices is formed at the body's trailing edge. The wake has an asymmetric behavior. The loss of energy is mainly due to the energy cascade.

Figure 57 exhibits the $-C_p$ distribution around the body wall obtained by the [2, 4] algorithms using the [8] turbulence model. The peak of C_p is 1.92 at the body's leading edge. The $-C_p$ plateau is well captured by both schemes. Figure 58 shows the turbulent kinetic energy profile at node 58. This plot shows that the Radespiel and Kroll (1995) scheme

captures more turbulent effects than the Van Leer (1982) scheme. The former transform more kinetic energy from the mean flow to turbulent movement scale.

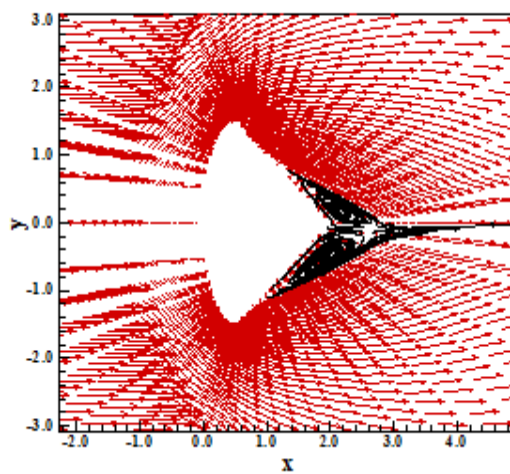


Figure 55. Velocity field and streamlines (VL-W).

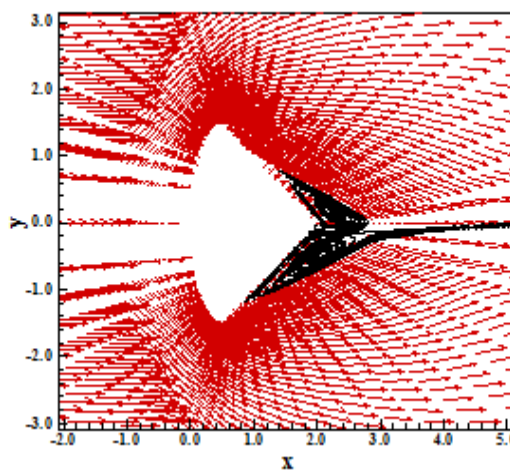


Figure 56. Velocity field and streamlines (RK-W).

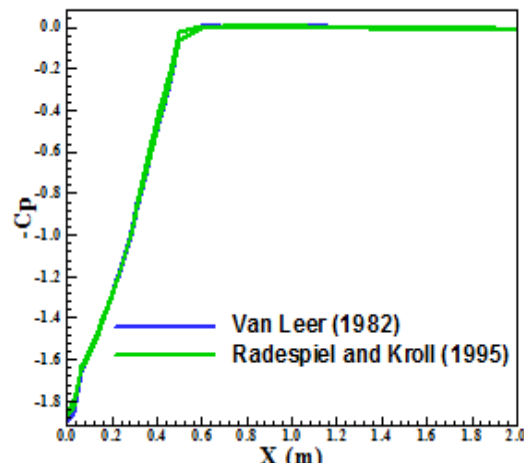


Figure 57. $-C_p$ distributions at wall.

Figure 59 exhibits the turbulent vorticity profile at node 58. As can be seen, the maximum dissipation through the vorticity generated by the vortices occurs at the body wall. It can reach the value 8.0×10^7 (dimensionless). These vortices results from the boundary layer separation and the formation of a pair of vortices at the wake. If the transient process was studied, it would be possible to accompany the propagation of the vortices from the trailing edge to the far field, through the vortex wake.

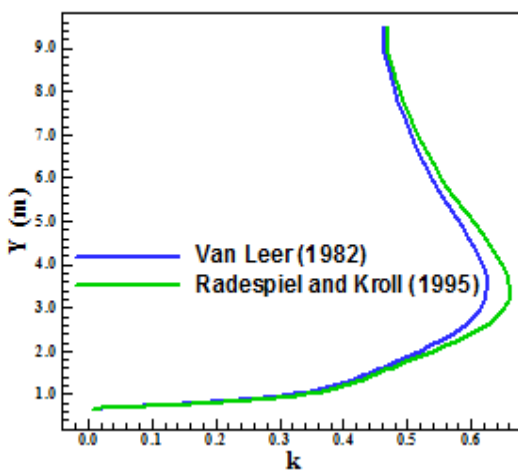


Figure 58. Turbulent kinetic energy.

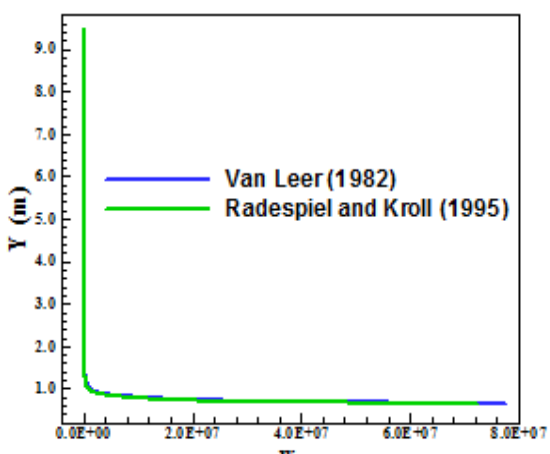


Figure 59. Turbulent vorticity.

Figure 60 shows the u profile at node 58. This profile is similar to the others, not presenting any meaningful difference. Moreover, the profile is typical of turbulent flows, justifying, hence, the employment of the turbulence models in this problem. It was highlighted in the figure the region close to the wall. It is possible to observe in Fig. 60 the reverse flow occurring (negative values of u). This reverse flow is clearer in Figs. 55 and 56. It is very interesting that, even in a separated region of fluid flow, the u profile maintain a monotonic

turbulent profile. This node (node 58) was chosen mainly due to the high level of energy that could be exchanged between the different and high/low energy levels of vortices. A truly energy cascade occurs in this region. This case is a moderate hypersonic “cold gas” flow and the turbulence is actually a reality. The next case is for a high hypersonic “cold gas” flow, being used an 11.0 Mach number. For this case, only the [8] model support the strength of the flow simulation, highlighting its robustness in relation to the others tested in this work.

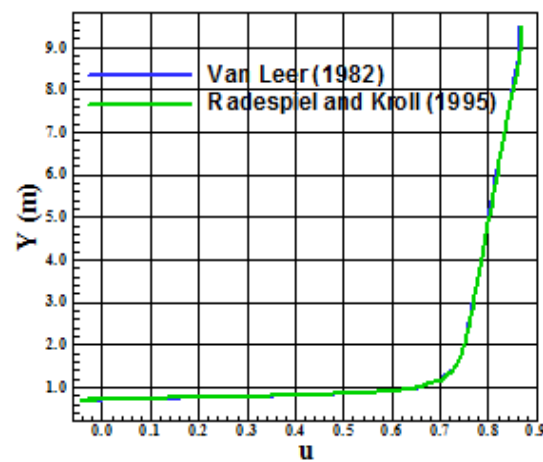


Figure 60. u profile.

Figures 61 and 62 present the pressure contours obtained by the [2, 4] schemes employing the [10] turbulence model. The pressure contours are clear, without oscillations. It is again observed that the [2] solution is more severe than the [4] solution, characterizing the former as more conservative.

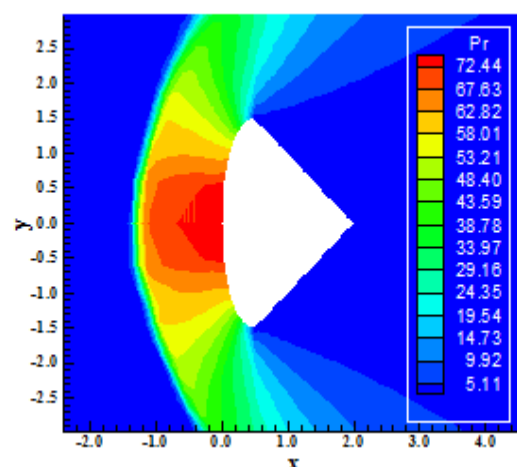
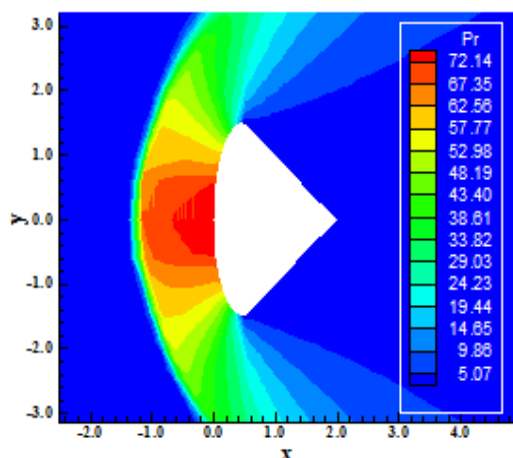
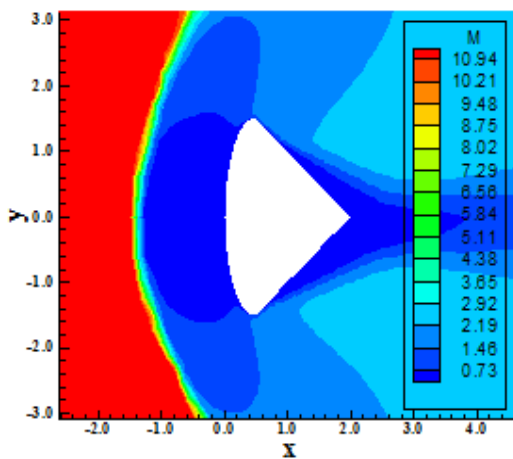
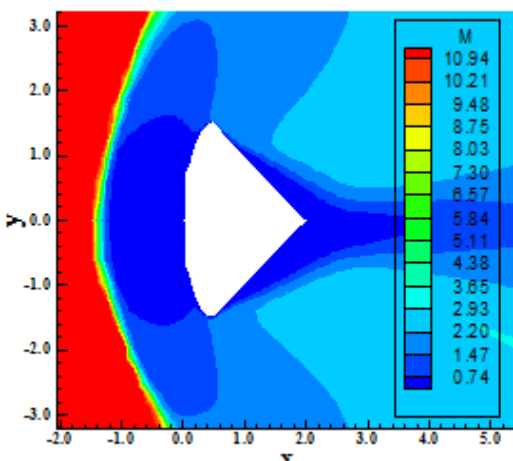


Figure 61. Pressure contours (VL-YGO).

**Figure 62. Pressure contours (RK-YGO).****Figure 63. Mach number contours (VL-YGO).****Figure 64. Mach number contours (RK-YGO).**

Figures 63 and 64 present the Mach number contours obtained by the [2, 4] schemes, respectively. As can be seen, the maximum Mach number reaches a value of 10.94 at freestream when

the exact value is 9.0. Both numerical schemes over-predict the Mach number field. The wake continues asymmetric, but the rest of the domain presents good symmetry characteristics.

Figures 65 and 66 exhibit the velocity field and the streamlines obtained by the [2, 4] schemes, respectively. Spite of the asymmetric behavior of the wake, the pair of vortices is well captured. The asymmetry seems more pronounced in the [4] scheme.

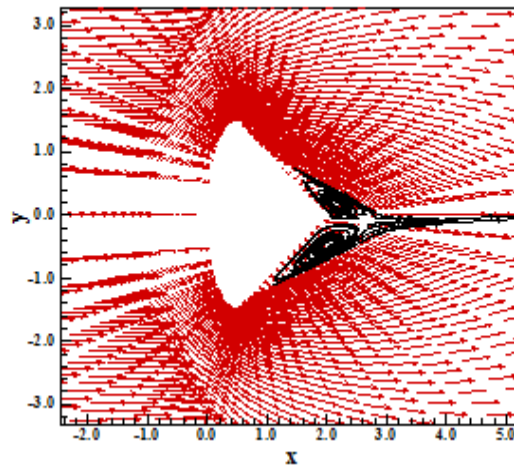
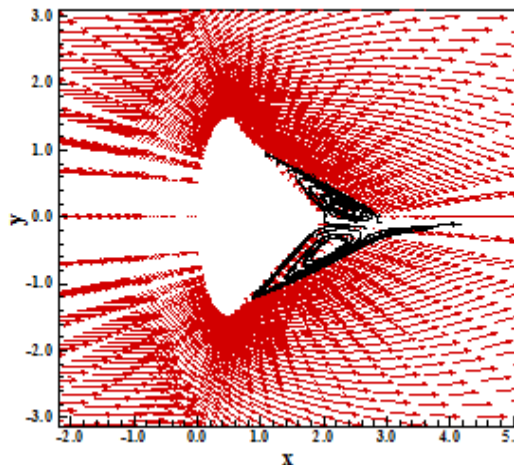
**Figure 65. Velocity field and streamlines (VL-YGO).****Figure 66. Velocity field and streamlines (RK-YGO).**

Figure 67 shows the $-C_p$ distribution around the geometry generated by the [2, 4] schemes using the [10] turbulence model. As can see, the differences between solutions are negligible. The C_p peak reaches a value of 1.92 and the C_p plateau is well captured.

Figure 68 exhibits the turbulent kinetic energy profile at node 58. This behavior consist in a smooth increase until 3.0m and after that a constant value until the far field.

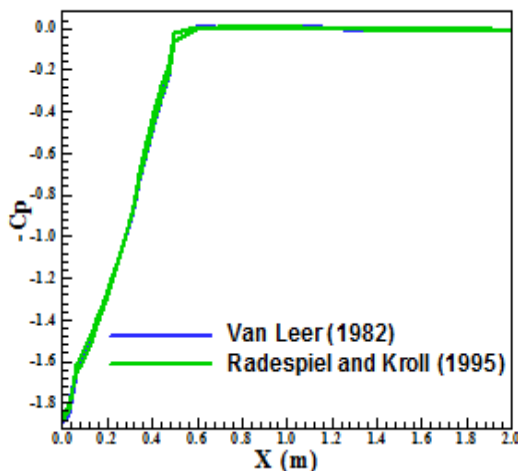
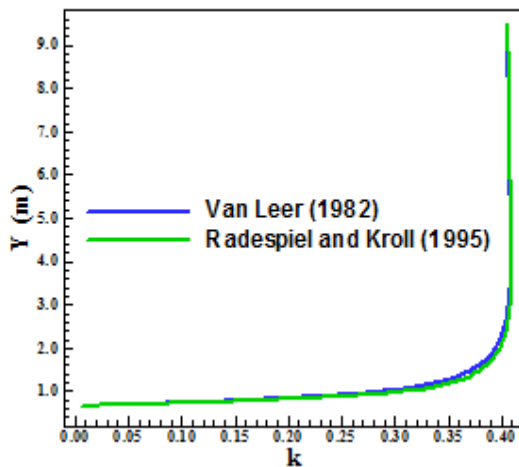
Figure 67. – C_p distributions at wall.

Figure 68. Turbulent kinetic energy.

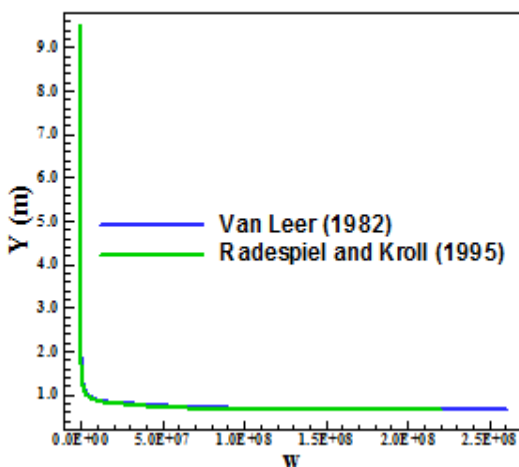


Figure 69. Turbulent vorticity.

Figure 69 presents the turbulent vorticity profile at node 58. The vorticity is zero far from the body. In approximately 1.0m above the body, the vorticity begin to increase due to the energy exchange among

vortices in the boundary layer. This increase in vorticity reaches its maximum close to the wall. Both numerical schemes predict the same behavior to the turbulent kinetic energy profile and to the turbulent vorticity profile.

Figure 70 presents the u profiles generated by the [2, 4] schemes. The u profile also maintains its description of the flow as turbulent.

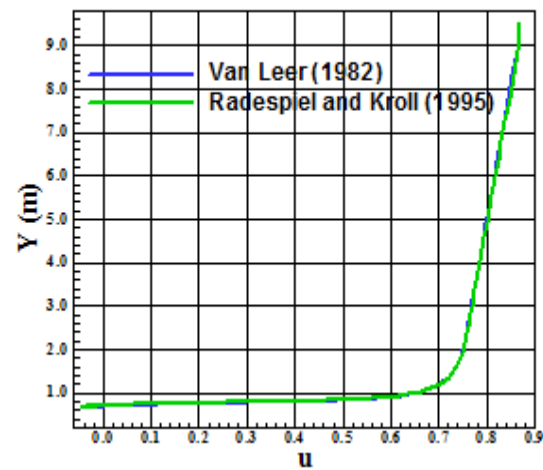


Figure 70. u profile.

Case 3 – $M = 11.0$ (High “cold gas” hypersonic flow). Figures 71 and 72 show the pressure contours obtained by the [2, 4] algorithms as they employ the [8] turbulence model. The pressure field generated by [2] solution is more severe than that generated by [4].

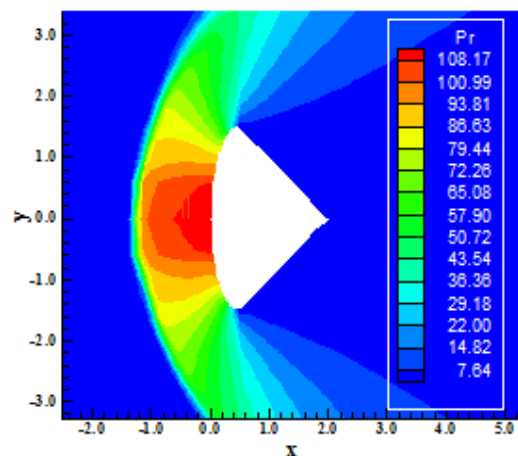


Figure 71. Pressure contours (VL-W).

Figures 73 and 74 present the Mach number contours obtained by the [2, 4] algorithms as using the [8] model to this high hypersonic flow. Both schemes simulate flows with freestream Mach number bigger than 16.0, which is an error because the original freestream Mach number used was 11.0.

It is possible to conclude that the turbulence model is generating this increase in the freestream Mach number. It happens at Mach 7.0, Mach 9.0 and now Mach 11.0.

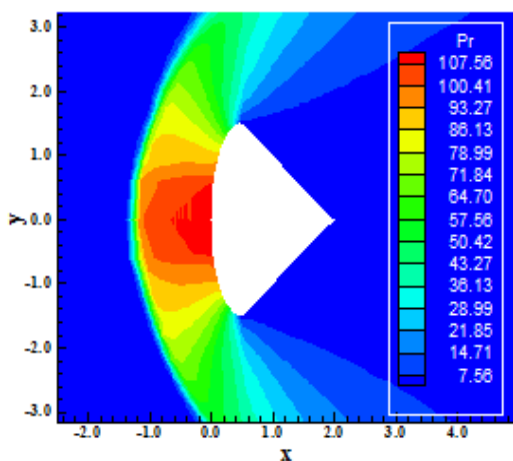


Figure 72. Pressure contours (RK-W).

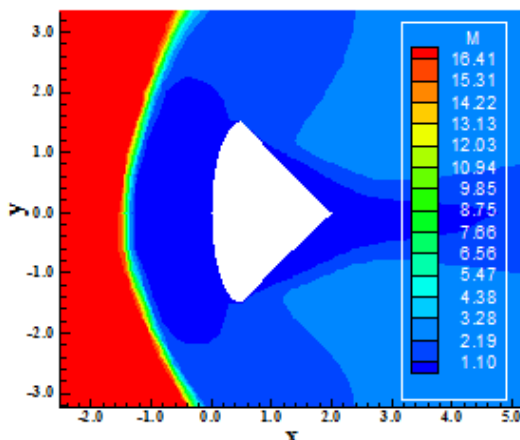


Figure 73. Mach number contours (VL-W).

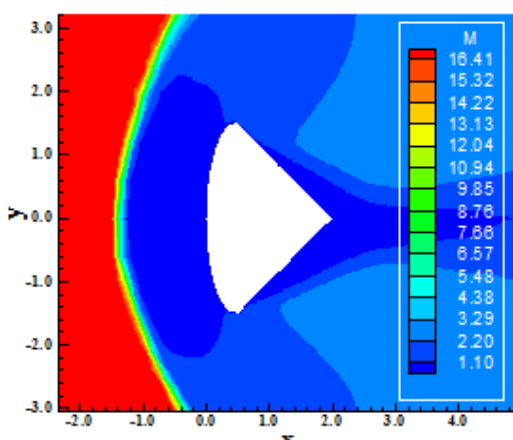


Figure 74. Mach number contours (RK-W).

Further study is necessary to determine where the error is in these simulations: error in numerical implementation or error in the turbulence model. It will be done in future, when these models and others were sufficient tested.

Figures 75 and 76 present the velocity field and the streamlines generated by the [2, 4] algorithms. As can be seen, there is non-symmetry in the vortices and at the wake. Both algorithms capture the shock wave as also the boundary layer detachment.

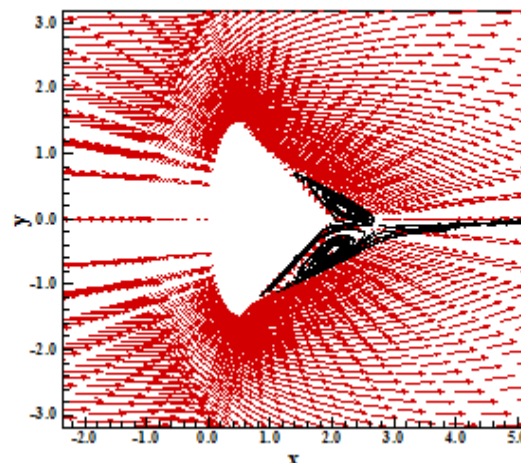


Figure 75. Velocity field and streamlines (VL-W).

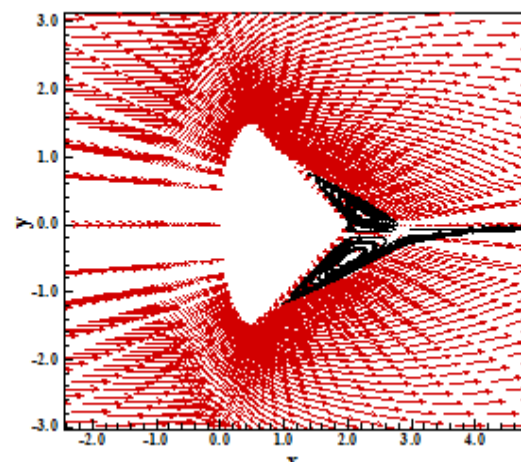


Figure 76. Velocity field and streamlines (RK-W).

Figure 77 shows the $-C_p$ distribution at wall obtained by the [2, 4] schemes. The peak of C_p is equal to 1.92, the same of the other cases. The C_p plateau is well defined. Both schemes capture this plateau.

Figure 78 presents the turbulent kinetic energy profile. It is a remarkable aspect that the two solutions, of different algorithms, coincide in this high hypersonic simulation. Figure 79 exhibits the turbulent vorticity profile. As can be seen, the

maximum vorticity occurs close to the wall and reaches values above 9.0×10^7 .

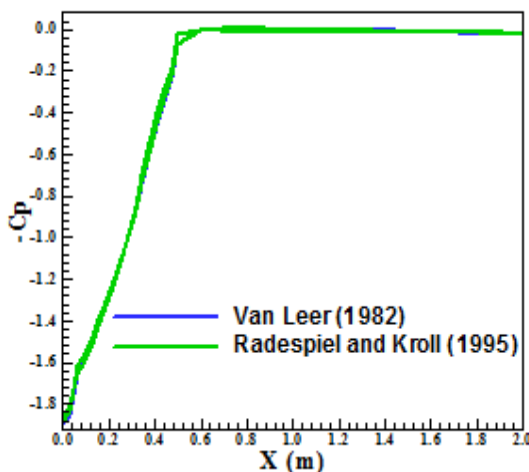


Figure 77. –Cp distributions at wall.

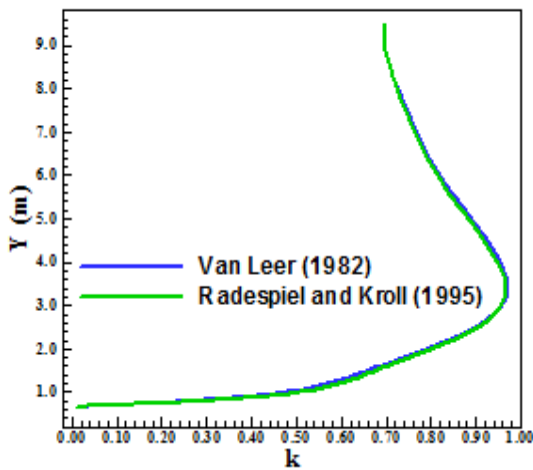


Figure 78. Turbulent kinetic energy.

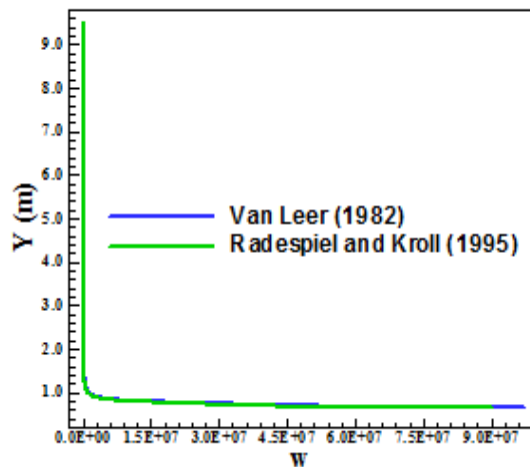


Figure 79. Turbulent vorticity.

Figure 80 shows the u profiles obtained by the [2, 4] algorithms. The u profile has the same characteristics of the cases before.

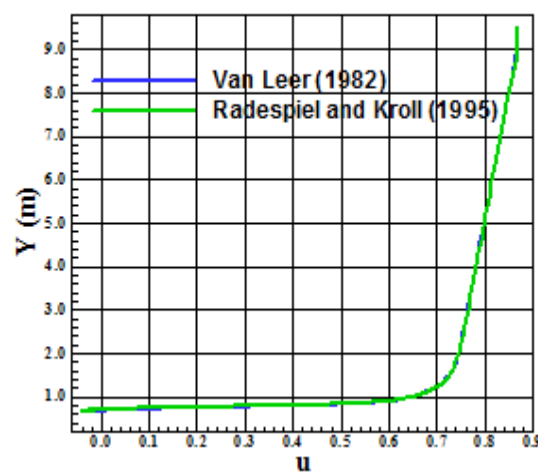


Figure 80. u profile.

2.2 Turbulent Solutions – Alternated Sense Mesh Generation

In this mesh generation process the [9] turbulence model could not be employed because its application depends of the normal distance from the wall to a cell under study. In this case, a row of cells is counted twice and the distance is applied to each cell. Hence, only the [8, 10] models are employed in this part of the present study. A detail of the mesh employed in the present study generated by the AS process is shown below:

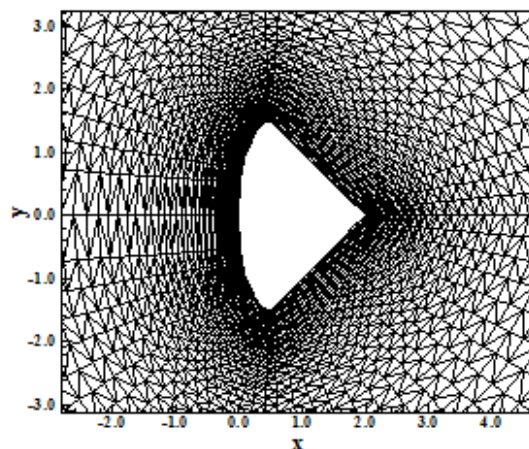


Figure 81. Re-entry capsule mesh (AS case).

Case 1 – $M = 9.0$ (Moderate “cold gas” hypersonic flow). Figures 82 and 83 exhibit the pressure contours obtained by the [2, 4] schemes, respectively, as using the [8] turbulence model. The pressure field generated by the [2] scheme is more intense than the respective one generated by the [4]

scheme. The shock wave is well captured by both algorithms. Figures 84 and 85 show the Mach number contours obtained by the [2, 4] algorithms, respectively, as using the [8] model. The Mach contours are more symmetrical at the wake. The peak of freestream Mach number is higher than the original freestream Mach number. It is a problem generated by the turbulence models and not a problem of the numerical schemes. The laminar hypersonic flow around this geometry is shown in [14] and it is clear that the solutions do not present Mach number peaks such as those found in this work.

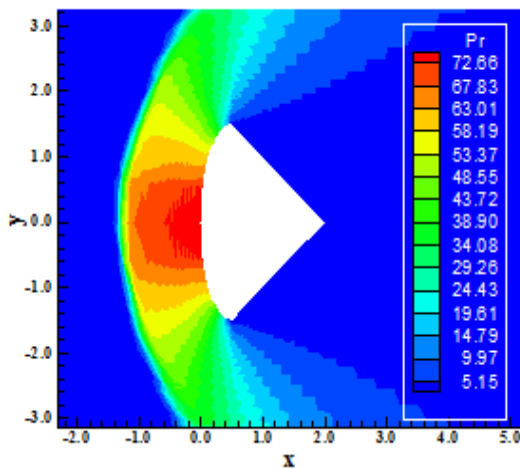


Figure 82. Pressure contours (VL-W).

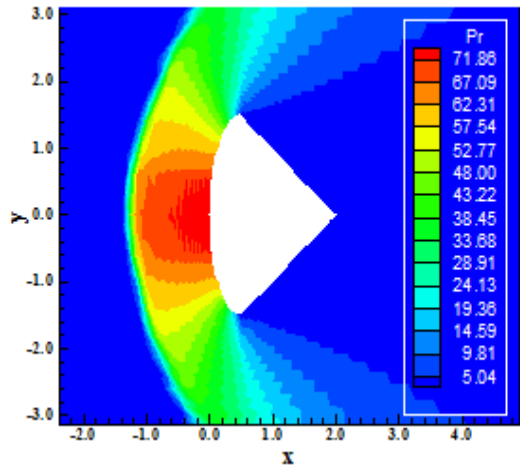


Figure 83. Pressure contours (RK-W).

Figures 86 and 87 show the velocity field and the streamlines obtained by the [2, 4] schemes as using the turbulence model of [8]. The pair of vortices is formed more symmetrically in relation to the body's symmetry axis. Moreover, the wake is positioned where it always should be: at the line of symmetry of the body. The vector field close to the wall

satisfies the adherence and impermeability conditions of the Navier-Stokes equations. As also can be seen, the shock wave is well captured by the schemes.

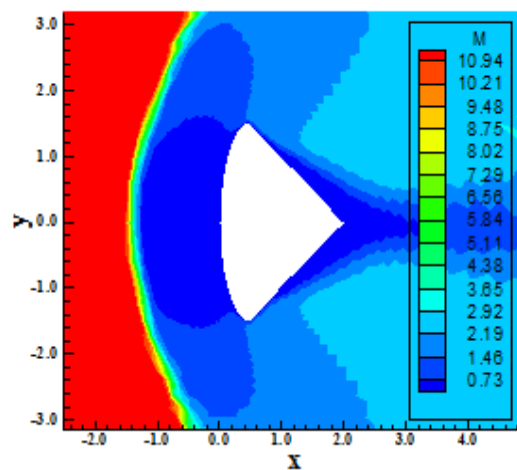


Figure 84. Mach number contours (VL-W).

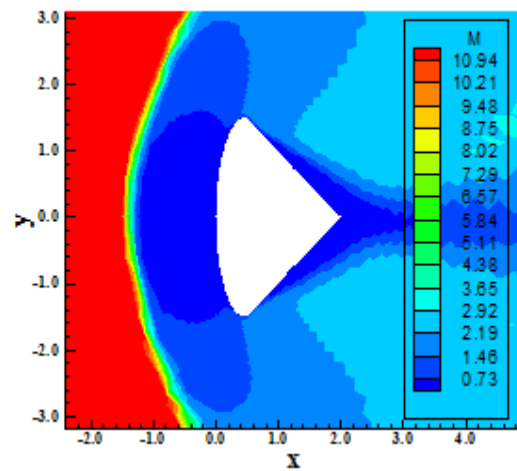


Figure 85. Mach number contours (RK-W).

Figure 88 shows the $-C_p$ distribution at wall obtained by the [2, 4] schemes as using the [8] turbulence model. The maximum peak of C_p is equal to 1.92. The C_p plateau is well captured. Both curves have similar behaviors. Figure 89 presents the turbulent kinetic energy profile at node 58. Both schemes practically captures the same profile, with the Radespiel and Kroll's solution a little more intense at $y = 4.0\text{m}$. Figure 90 exhibits the turbulent vorticity profile at node 58. The maximum value of vorticity is obtained close to the wall and has the approximate value of 8.0×10^7 . It can be seen that the vorticity is equal to zero in the mean flow and assumes values different of zero only close to the wall, where the pair of vortices generate excessive exchange of energy and the vorticity is increased to

factors of 10^7 , as in this example. The cascade of energy is well characterized in this context.

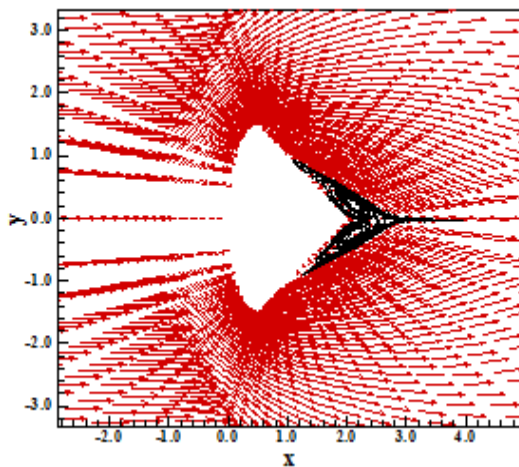


Figure 86. Velocity field and streamlines (VL-W).

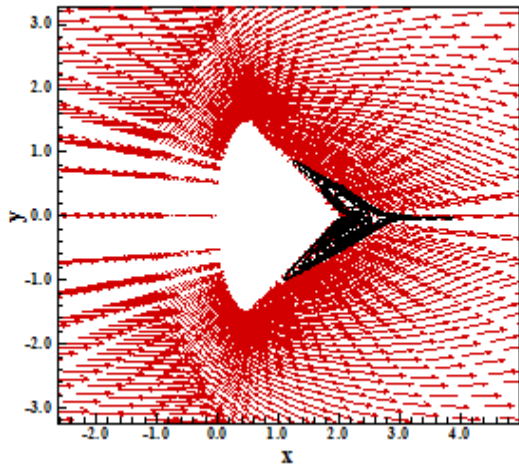


Figure 87. Velocity field and streamlines (RK-W).

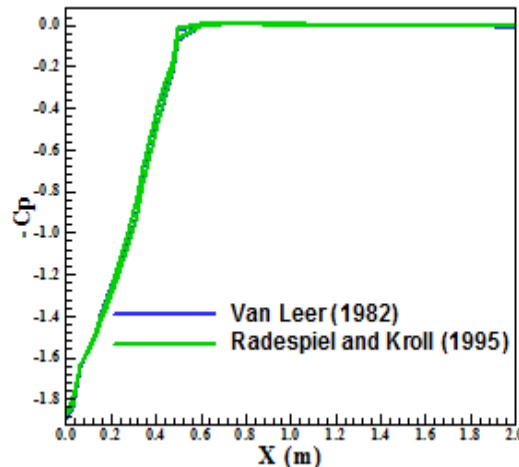


Figure 88. -Cp distributions at wall.

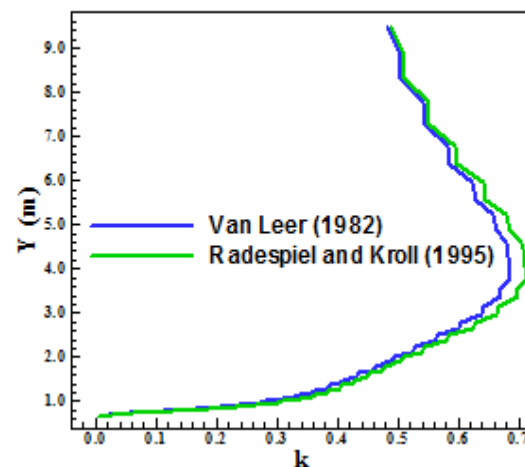


Figure 89. Turbulent kinetic energy.

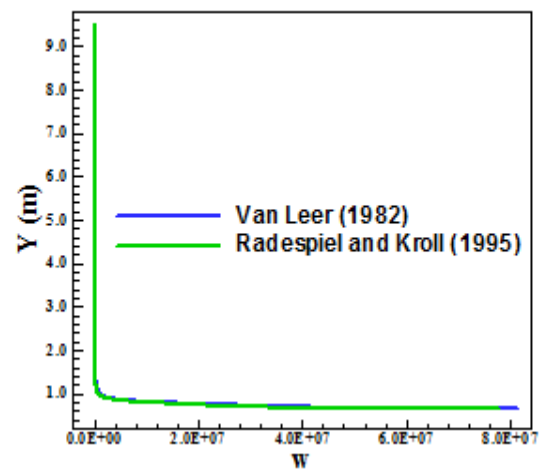


Figure 90. Turbulent vorticity.

Figure 91 exhibits the u profile. Its agreement to the turbulent profile is conclusive. There is a reverse flow close to the wall captured by the schemes.

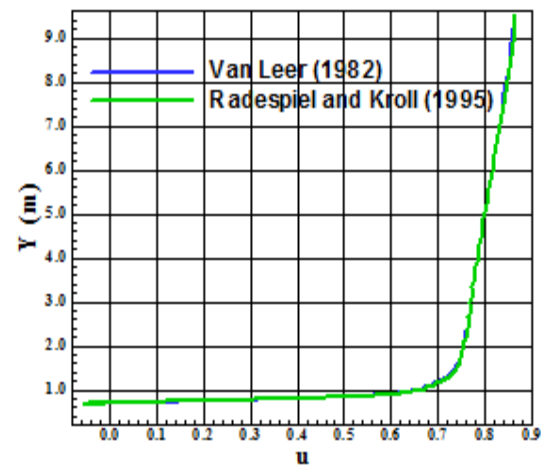


Figure 91. u profile.

Figures 92 and 93 present the pressure contours obtained by the [2, 4] schemes as employing the [10] turbulence model. The pressure field generated by the [2] scheme is more intense than the respective one generated by the [4] scheme. Both solutions present good symmetry properties.

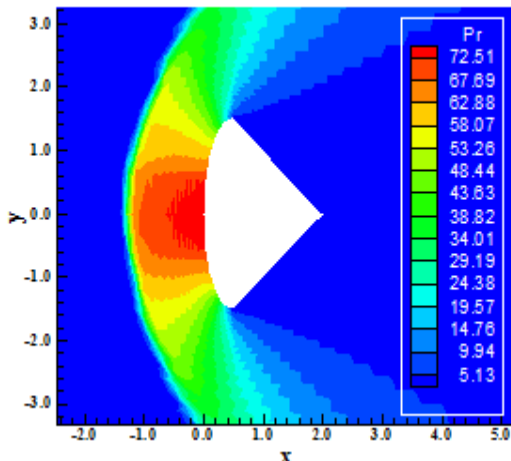


Figure 92. Pressure contours (VL-YGO).

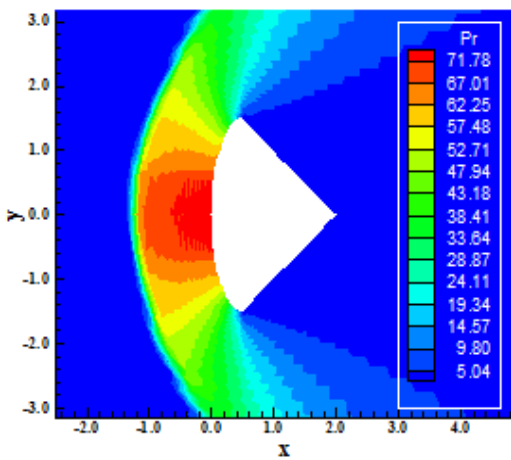


Figure 93. Pressure contours (RK-YGO).

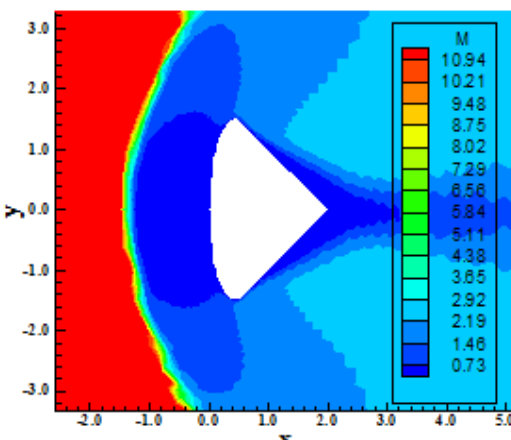


Figure 94. Mach number contours (VL-YGO).

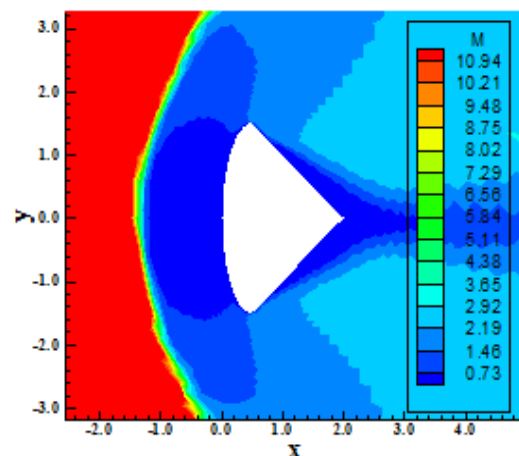


Figure 95. Mach number contours (RK-YGO).

Figures 94 and 95 show the Mach number contours obtained by the [2, 4] schemes as using the [10] turbulence model. It is possible to observe in these figures that the wake is positioned more symmetrically in relation to the body's symmetry line. The shock wave is well captured by both schemes.

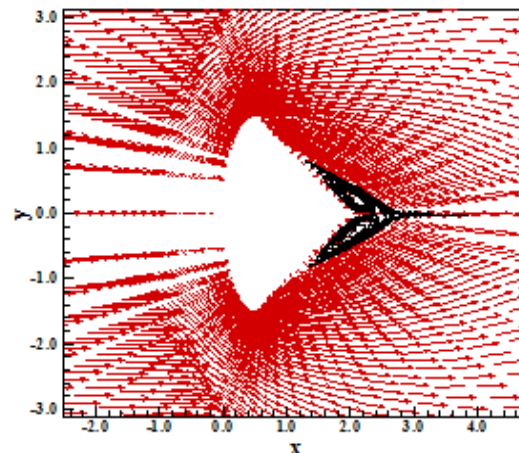


Figure 96. Velocity field and streamlines (VL-YGO).

Figure 96 and 97 exhibit the velocity vector field and the streamlines generated by the [2, 4] schemes. Both algorithms capture the boundary layer separation and the formation of the pair of vortices at the body's trailing edge. The vortices are symmetrically positioned in relation to the body's symmetry line and it results that the wake is also aligned with body's axis.

Figure 98 shows the $-C_p$ distributions at wall obtained by the numerical schemes. Both algorithms detect a C_p peak of 1.92 at the body's leading edge and the C_p plateau is well defined. Figure 99 presents the turbulent kinetic energy profiles at node

58 obtained by the [2, 4] schemes using the turbulence model of [10]. The solutions are very close, with none significant difference. After 4.0m the turbulent kinetic energy tends to be constant and equal to 0.41 (dimensionless).

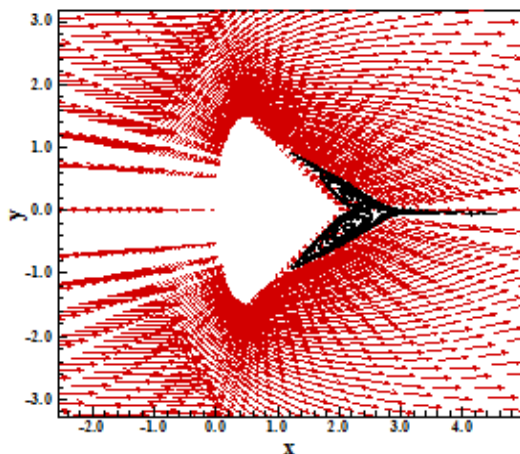


Figure 97. Velocity field and streamlines (RK-YGO).

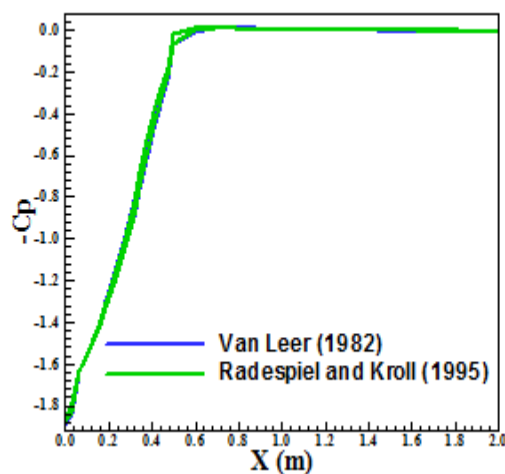


Figure 98. $-C_p$ distributions at wall.

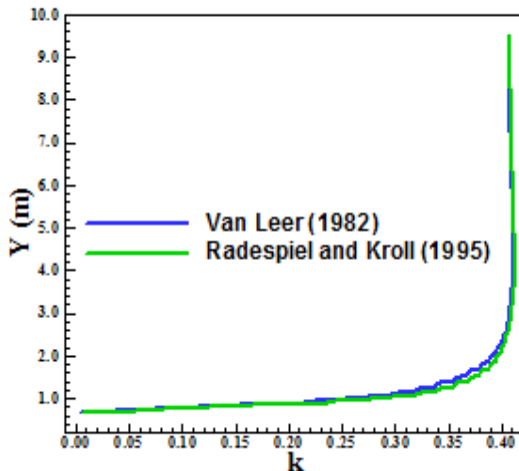


Figure 99. Turbulent kinetic energy.

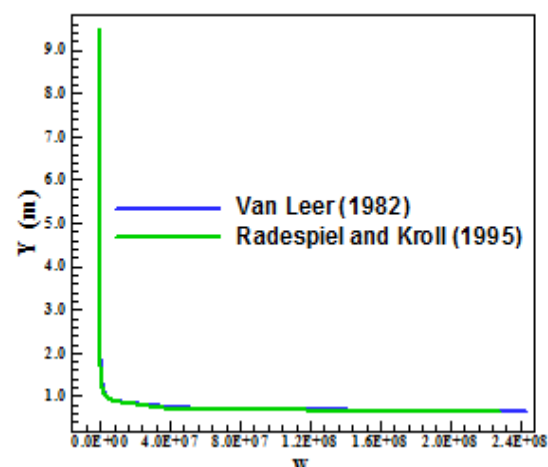


Figure 100. Turbulent vorticity.

Figure 100 exhibits the turbulent vorticity profile at node 58 generated by the turbulence model under study. This profile presents the typical behavior of the turbulent vorticity field: close to the wall assumes a maximum and far from the wall assumes the value zero. The two levels of energy – production and dissipation – present the expected behavior. Both algorithms and turbulence model yield the appropriate description of the flowfield.

Figure 101 exhibits the u profile at node 58. Both solutions generated by the [2, 4] algorithms are practically the same. The u component of velocity obeys the turbulent profile obtained in a turbulent flow.

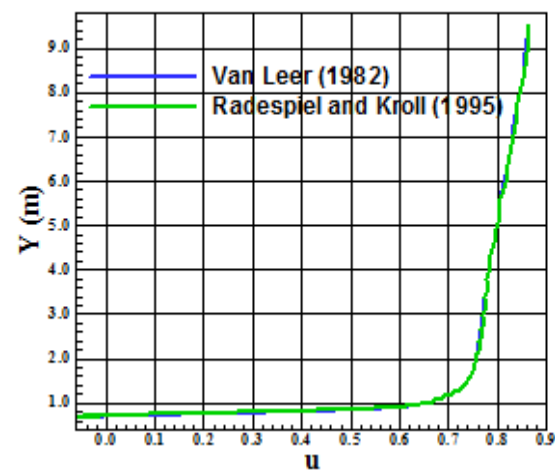


Figure 101. u profile.

Case 2 – $M = 11.0$ (High “cold gas” hypersonic flow). Figures 102 and 103 exhibit the pressure contours obtained by the [2, 4] algorithms employing the [8] turbulence model. The pressure field generated by the [2] scheme is more severe

than the respective generated by the [4] scheme. It characterizes the [2] scheme as more conservative than the [4] scheme.

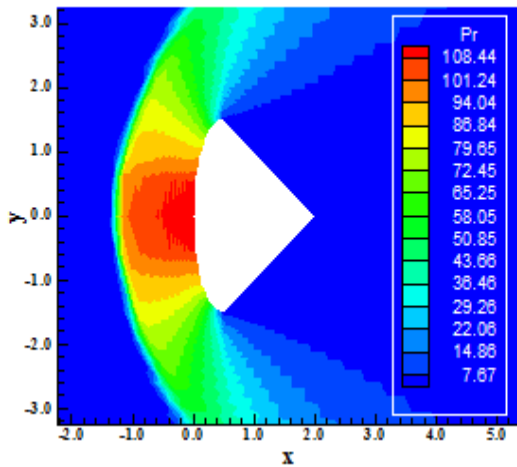


Figure 102. Pressure contours (VL-W).

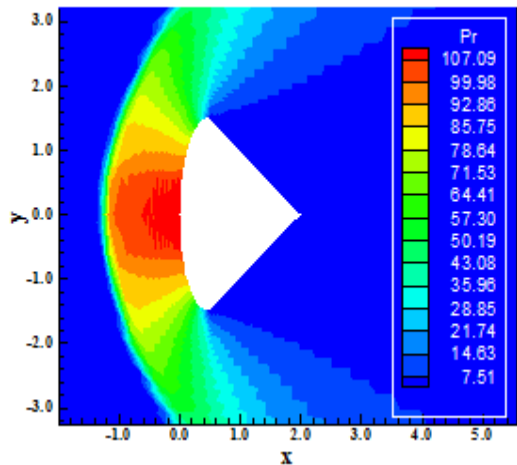


Figure 103. Pressure contours (RK-W).

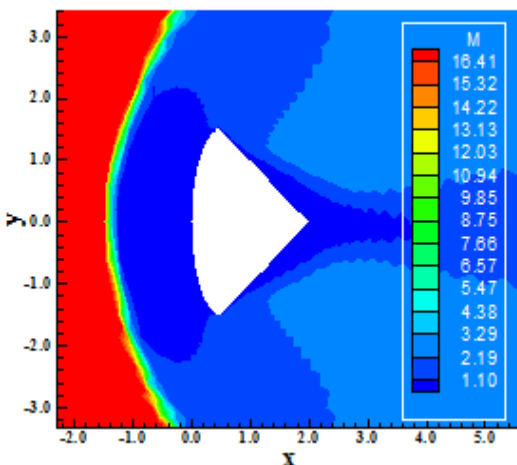


Figure 104. Mach number contours (VL-W).

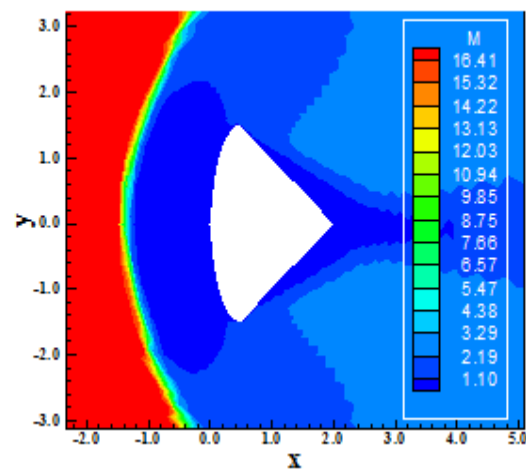


Figure 105. Mach number contours (RK-W).

Figures 104 and 105 show the Mach number contours obtained by the [2, 4] schemes as using the [8] turbulence model. The Mach number peak is far from the original freestream Mach number. It means that there is an incorrect implementation or the turbulence models are generating such behavior. More studies are necessary to better distinguish this aspects of the turbulence models. It is not a problem of the numerical schemes, as can be assured in [14]. The wake is formed and is aligned with the body's symmetry axis.

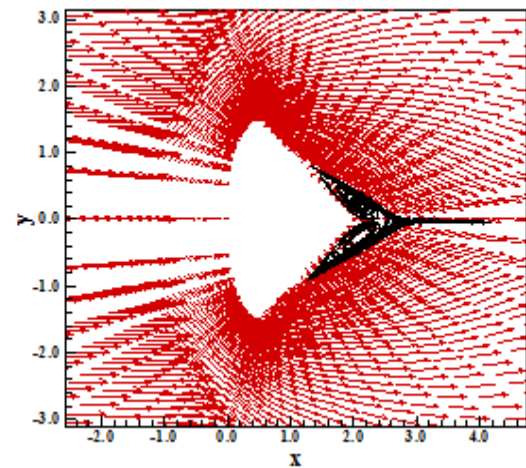


Figure 106. Velocity field and streamlines (VL-W).

Figures 106 and 107 present the velocity field and the streamlines obtained by the numerical algorithms of [2, 4], employing the [8] turbulence model. The vortices distribution is symmetric in relation to the body's symmetry axis. The wake is aligned with the body's symmetry axis. The adherence and impermeability conditions required by the Navier-Stokes equations are plenty satisfied. The boundary layer separation and the shock wave

are well captured by the numerical algorithms, which ratifies these ones as efficient numerical tools to be used in absence of a high resolution scheme. They are upwind schemes with good capturing properties of the flow discontinuity.

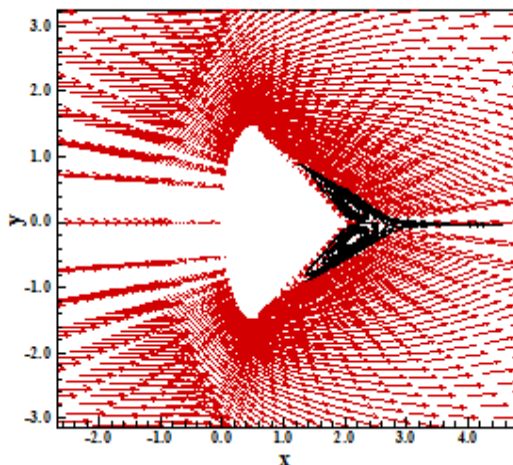


Figure 107. Velocity field and streamlines (RK-W).

Figure 108 exhibits the $-C_p$ distributions at wall obtained by the [2, 4] algorithms as using the [8] turbulence model. The peak of C_p is equal to 1.92, the same obtained in all simulations. The C_p plateau is also captured, as occurred in all studied cases of this work. Both solutions – [2, 4] – present similar behavior, not being possible identify one better than the other.

Figure 109 presents the turbulent kinetic energy profile generated by the numerical schemes under study, using the [8] turbulence model. There are small differences between the solutions. The [4] scheme characterizing the flow a little more turbulent than the [2] scheme does. In quantitative terms, the difference is small.

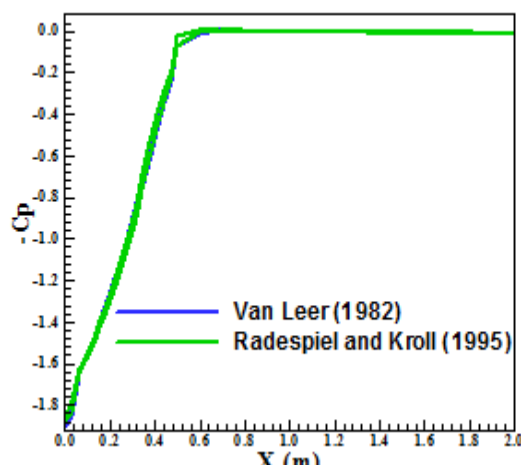


Figure 108. $-C_p$ distributions at wall.

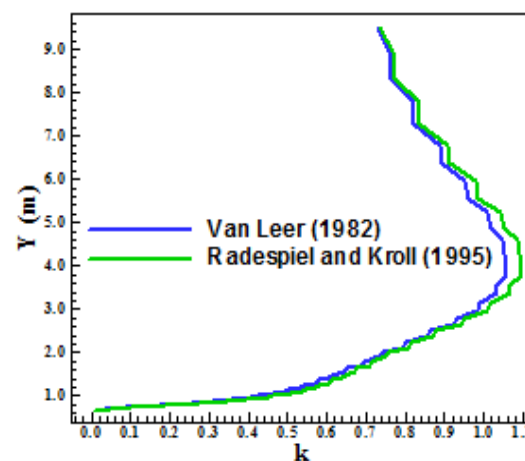


Figure 109. Turbulent kinetic energy.

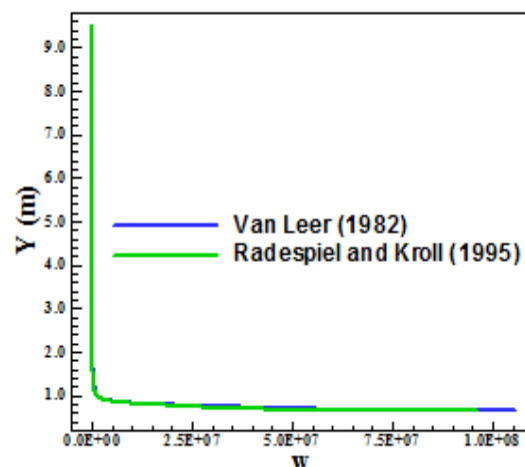


Figure 110. Turbulent vorticity.

Figure 110 shows the turbulent vorticity profile obtained by the [2, 4] algorithms employing the [8] turbulence model. The biggest value of vorticity is found close to the wall and assumes a dimensionless value of 10^8 . Far from the wall the vorticity is zero because there are no vortices at the far field. The local of great exchange of energy, due to the cascade of energy, is close to the wall, where the vortices are created and propagated, interacting among themselves.

Figure 111 exhibits the u profile. This dimensionless profile is typical of a turbulent flow, indicating that the present study is valid. A reverse flow region is identified by both algorithms close to the wall. This region was observed in others similar solutions studied in this work. The cut off behavior observed in some profiles is due to the mesh generation process. Note that in the SS case, the cut off effect is not present. It is due to the continuity in the ordination of the cells and neighbors. In the AS case this ordination is more spread out. The good

solution aspects observed in this work, in the inviscid and turbulent flows, justify such use and ratify the affirmation done in [14].

2.3 Stagnation Pressure Estimation

One possibility to quantitative comparison of both schemes and all turbulence models is the determination of the stagnation pressure ahead of the configuration. [15] presents a table of normal shock wave properties in its B Appendix. This table permits the determination of some shock wave properties as function of the freestream Mach number. In front of the re-entry capsule configuration, the shock wave presents a normal shock behavior, which permits the determination of the stagnation pressure, behind the shock wave, from the tables encountered in [15]. It is possible to determine the ratio pr_0/pr_∞ from [15], where pr_0 is the stagnation pressure in front of the configuration and pr_∞ is the freestream pressure (equals to $1/\gamma$ with the present dimensionless). Hence, to the three cases studied in this work, Tab. 1 gives:

Table 1. Theoretical values of pr_0 .

Mach	pr_0/pr_∞	pr_∞	pr_0
7.0	63.55	0.714	45.37
9.0	104.80	0.714	74.83
11.0	156.30	0.714	111.60

Table 2. Values of stagnation pressure – Mach = 7.0 (SS).

Scheme	Model	pr_0	Error (%)
[2]	Wilcox	44.23	2.51
	MR – W	44.23	2.51
	MR – TL	44.23	2.51
	MR – BSL	44.23	2.51
	MR – SST	44.23	2.51
	YGO	44.11	2.78
[4]	Wilcox	43.73	3.61
	MR – W	43.73	3.61
	MR – TL	43.73	3.61
	MR – BSL	43.73	3.61
	MR – SST	43.73	3.61
	YGO	43.02	5.18

Table 2 shows the values of the stagnation pressure obtained by the [2, 4] to the three turbulence models studied in this work for the case $M_\infty = 7.0$. Errors less than 5.20% were found. The best results were obtained with the [2] scheme using the [8-9], in all variants, turbulence models. Table 3 presents the values of the stagnation pressure

obtained by the [2, 4] schemes as using the [8, 10] turbulence models for the case $M_\infty = 9.0$. Errors less than 4.10% were found. The best result was obtained with the [2] scheme using the [8] turbulence model. Finally, in Table 4 is presented the values of the stagnation pressure obtained by the [2, 4] as using the [8] turbulence model for the case $M_\infty = 11.0$. Errors less than 3.70% were found. The best result was obtained with the [2] scheme. All these results are to a Same Sense (SS) mesh generation process.

Table 3. Values of stagnation pressure – Mach = 9.0 (SS).

Scheme	Model	pr_0	Error (%)
[2]	Wilcox	72.60	2.98
	YGO	72.44	3.19
[4]	Wilcox	71.82	4.02
	YGO	72.14	3.59

Table 4. Values of stagnation pressure – Mach = 11.0 (SS).

Scheme	Model	pr_0	Error (%)
[2]	Wilcox	108.17	3.07
[4]	Wilcox	107.56	3.62

For a Alternated Sense (AS) mesh generation process, one has in Tab. 5 the values of the stagnation pressure obtained by the [2, 4] as using the [8, 10] turbulence models for the case $M_\infty = 9.0$. Errors less than 4.10% were found. The best result was obtained with the [2] scheme using the [8] turbulence model. Table 6 presents the values of the stagnation pressure obtained by [2, 4] as using the [8] turbulence model for the case $M_\infty = 11.0$. Errors less than 4.10% were found. The best result was obtained with the [2] scheme.

Table 5. Values of stagnation pressure – Mach = 9.0 (AS).

Scheme	Model	pr_0	Error (%)
[2]	Wilcox	72.66	2.90
	YGO	72.51	3.10
[4]	Wilcox	71.86	3.97
	YGO	71.78	4.06

Table 6. Values of stagnation pressure – Mach = 11.0 (AS).

Scheme	Model	pr_0	Error (%)
[2]	Wilcox	108.44	2.83
[4]	Wilcox	107.09	4.04

2.4 Turbulent Viscous Conclusions

As conclusion of the turbulent viscous calculations it is possible to affirm that the [2] scheme is more conservative than the [4] scheme. The former is also more accurate in the determination of the stagnation pressure at the configuration nose. It is also possible to conclude that the [8] turbulence model is the most robust among the tested models. The [9], in its four variants, presented limited robustness properties, but it is also as accurate as the [8] model is. The [10] turbulence model is an intermediate one: better than the [9] in terms of robustness and worse than the [8] in terms of accuracy. The best turbulence model in terms of accuracy was the [8] one, with errors below 4.10% in the estimation of the stagnation pressure ahead of the re-entry capsule configuration. The AS mesh generation process was again the most appropriate choose to yield meshes of good quality, in terms of symmetry and in the determination of the shock wave thickness. The reducing in the shock wave thickness and the good distribution of the vortices in relation to the body's symmetry line are highlighted aspects of this process and guarantees or ratify such choose when treating unstructured spatial discretization.

3 Conclusions

In this work, the forth of this study, numerical simulations involving supersonic and hypersonic flows on an unstructured context are analysed. The [2, 4] schemes are implemented on a finite volume formulation, using unstructured spatial discretization. The algorithms are implemented in their first and second order spatial accuracies. The second order spatial accuracy is obtained by a linear reconstruction procedure based on the work of [6]. Several non-linear limiters are studied using the linear interpolation based on the work of [7]. To the turbulent simulations, the [8-10] models are employed. The compression corner problem to the inviscid simulations and the re-entry capsule problem to the hypersonic viscous simulations are studied. The results have demonstrated that the [2] algorithm yields the best results in terms of the prediction of the shock angle of the oblique shock wave in the compression corner problem and the best value of the stagnation pressure at the configuration nose in the re-entry capsule configuration. The spatially variable time step is the best choice to accelerate the convergence of the numerical schemes, as reported by [11-12]. In terms of turbulent results, the [8] model yields the best results, proving the good capacity of this turbulence

model in simulate high hypersonic flows. This paper is continuation of Maciel's works started in 2011 and treats mainly the influence of turbulence models on the solution quality.

4 Acknowledgments

The author acknowledges the CNPq by the financial support conceded under the form of a DTI (Industrial Technological Development) scholarship no. 384681/2011-5. He also acknowledges the infrastructure of the ITA that allowed the realization of this work.

References:

- [1] P. Kutler, Computation of Three-Dimensional, Inviscid Supersonic Flows, *Lecture Notes in Physics*, Vol. 41, 1975, pp. 287-374.
- [2] B. Van Leer, Flux-Vector Splitting for the Euler Equations, *Proceedings of the 8th International Conference on Numerical Methods in Fluid Dynamics*, E. Krause, Editor, Lecture Notes in Physics, Vol. 170, 1982, pp. 507-512, Springer-Verlag, Berlin.
- [3] M. Liou, and C. J. Steffen Jr., A New Flux Splitting Scheme, *Journal of Computational Physics*, Vol. 107, 1993, pp. 23-39.
- [4] R. Radespiel, and N. Kroll, Accurate Flux Vector Splitting for Shocks and Shear Layers, *Journal of Computational Physics*, Vol. 121, 1995, pp. 66-78.
- [5] P. L. Roe, Approximate Riemann Solvers, Parameter Vectors, and Difference Schemes, *Journal of Computational Physics*, Vol. 43, 1981, pp. 357-372.
- [6] T. J. Barth, and D. C. Jespersen, The Design and Application of Upwind Schemes on Unstructured Meshes, *AIAA Paper 89-0336*, 1989.
- [7] F. Jacon, and D. Knight, A Navier-Stokes Algorithm for Turbulent Flows Using an Unstructured Grid and Flux Difference Splitting", *AIAA Paper 94-2292*, 1994.
- [8] D. C. Wilcox, Reassessment of the Scale-Determining Equation for Advanced Turbulence Models, *AIAA Journal*, Vol. 26, No. 11, 1988, pp. 1299-1310.
- [9] F. R. Menter, and C. L. Rumsey, Assessment of Two-Equation Turbulence Models for Transonic Flows, *AIAA Paper 94-2343*, 1994.
- [10] D. A. Yoder, N. J. Georgiadis, and P. D. Orkwis, Implementation of a Two-Equation k-

- omega turbulence model in NPARC, *AIAA Paper 96-0383*, 1996.
- [11] E. S. G. Maciel, Analysis of Convergence Acceleration Techniques Used in Unstructured Algorithms in the Solution of Aeronautical Problems – Part I, *Proceedings of the XVIII International Congress of Mechanical Engineering (XVIII COBEM)*, Ouro Preto, MG, Brazil, 2005.
- [12] E. S. G. Maciel, Analysis of Convergence Acceleration Techniques Used in Unstructured Algorithms in the Solution of Aerospace Problems – Part II, *Proceedings of the XII Brazilian Congress of Thermal Engineering and Sciences (XII ENCIT)*, Belo Horizonte, MG, Brazil, 2008.
- [13] E. S. G. Maciel, Supersonic and Hypersonic Flows on 2D Unstructured Context: Part III Others Turbulence Models, Submitted to *WSEAS Transactions on Applied and Theoretical Mechanics* (under review).
- [14] E. S. G. Maciel, Supersonic and Hypersonic Flows on 2D Unstructured Context: Part II, *WSEAS Transactions on Fluid Dynamics*, Vol. 6, October, Issue 4, 2011, pp. 227-256.
- [15] J. D. Anderson Jr., *Fundamentals of Aerodynamics*, McGraw-Hill, Inc., 563p, 1984.